CHALMERS
UNIVERSITY OF TECHNOLOGY

# Aerodynamic investigation of a vehicle in highly turbulent flow

Master's thesis in Mobility Engineering

Pedro John
Salvatore Verde

Department of Mechanics and Maritime Sciences

CHALMERS UNIVERSITY OF TECHNOLOGY
Gothenburg, Sweden 2025
www.chalmers.se

Master's thesis 2025

# Aerodynamic investigation of a vehicle in highly turbulent flow

Pedro John, Salvatore Verde


CHALMERS
UNIVERSITY OF TECHNOLOGY

Department of Mechanics and Maritime Sciences
*Division of Vehicle Engineering and Autonomous Systems*
Chalmers University of Technology
Gothenburg, Sweden 2025

Aerodynamic investigation of a vehicle in highly turbulent flow
PEDRO JOHN
SALVATORE VERDE



Supervisor: Alexey Vdovin, Vehicle Engineering and Autonomous Systems
Examiner: Alexey Vdovin, Vehicle Engineering and Autonomous Systems

Master's Thesis 2025
Department of Mechanics and Maritime Science
Division of Vehicle Engineering and Autonomous Systems
Chalmers University of Technology
SE-412 96 Gothenburg
Telephone +46 31 772 1000

Cover: Active turbulence generator mounted in the wind tunnel with all necessary components.

Typeset in LaTeX
Printed by Chalmers Reproservice
Gothenburg, Sweden 2025

Aerodynamic investigation of a vehicle in highly turbulent flow
SALVATORE VERDE
PEDRO JOHN
Department of Mechanics and Maritime Science
Chalmers University of Technology

# Abstract

This master's thesis presents the design, simulation, and experimental validation of an active turbulence generator aimed at reproducing realistic, highly turbulent flow conditions for vehicle aerodynamic testing in a scale wind tunnel. The main goal is to bridge the gap between idealized wind tunnel tests and the unsteady, turbulent flow scenarios encountered during real-world highway and urban driving. To achieve this, an active turbulence generator using oscillating airfoils was developed. The airfoils, based on the NACA 0015 profile, were actuated to produce adjustable turbulence intensities and length scales, matching conditions such as turbulence intensities of 1–5% for highway speeds in real-world driving scenarios. Computational Fluid Dynamics (CFD) simulations were conducted using the $\kappa - \omega$ SST turbulence model with an overset mesh technique to accurately resolve the unsteady interaction between the moving airfoils and the freestream. The simulations analyzed characteristic parameters including turbulence intensity, turbulent length scale distributions, and aerodynamic loads on a DrivAer reference model. The design was optimized to ensure turbulence generation across the test section while keeping the required mechanical power within feasible limits. A mechanical system driven via a single motor through a chain was designed and manufactured using rapid prototyping techniques, allowing synchronized oscillatory motion of all seven airfoils. The system was integrated into the Chalmers scale wind tunnel and tested. The findings serve as a solid foundation to be built upon in future projects regarding the development of an active turbulence generator.

Keywords: wind tunnel, turbulence generator, DrivAer, active turbulence

# Acknowledgements

We would like to express our deepest gratitude to our supervisor, Alexey Vidovin, for his ongoing support and guidance throughout this research project. We would also like to thank FUSE Labs for their support during the manufacturing phase, as well as for their valuable insights on specific components. Finally, we would like to thank our family and friends for their constant encouragement and support throughout this journey.

Pedro John and Salvatore Verde, Gothenburg, June 2025

# List of Acronyms

Below is the list of acronyms that have been used throughout this thesis listed in alphabetical order:

| | |
|---|---|
| CFD | Computational Fluid Dynamics |
| DNS | Direct Numerical Simulation |
| FEM | Finite Element Method |
| HRN | High Reynolds Number |
| LES | Large Eddy Simulation |
| LRN | Low Reynolds Number |
| NACA | National Advisory Committee for Aeronautics |
| NASA | National Aeronautics and Space Administration |
| RANS | Reynolds-Averaged Navier-Stokes |
| Re | Reynolds Number |
| $Re_{crit}$ | Critical Reynolds Number |
| $Re_T$ | Turbulent Reynolds Number |
| SGS | Subgrid Scale |
| TUM | Technical University of Munich |

# Nomenclature

Below is the nomenclature of parameters that have been used throughout this thesis.

## Parameters

| | |
|---|---|
| $\rho$ | Density |
| $v$ | Velocity |
| $l$ | Characteristic Length |
| $\mu$ | Viscosity |
| $\eta$ | Kolmogorov Length Scale |
| $\nu$ | Kinematic Viscosity |
| $\epsilon$ | Turbulent Dissipation Rate |
| $\kappa$ | Turbulent Kinetic Energy |
| $\hat{E}$ | Energy Spectrum |
| $I$ | Turbulence Intensity |
| $u'$ | Root Mean Square Of The Turbulent Velocity |
| $U$ | Mean Velocity |
| $p$ | Pressure |
| $t$ | Time |
| $u$ | Velocity in X-Direction |
| $v$ | Velocity in Y-Direction |
| $w$ | Velocity in Z-Direction |
| $\mathbf{u}$ | Velocity in X,Y,Z-Direction |
| $\phi$ | Flow quantity |
| $\bar{\phi}$ | Time-averaged component |
| $\phi'$ | Fluctuating component |
| $l_t$ | Turbulent Length Scale |
| $d_n$ | Distance to the nearest Wall |

| | |
|---|---|
| $\omega$ | Specific Dissipation Rate |
| $u^+$ | Dimensionless Velocity |
| $y^+$ | Dimensionless Wall Distance |
| $u_\tau$ | Friction Velocity |
| $\tau_w$ | Wall Shear Stress |
| $C$ | Integration Constant |
| $\mu_t$ | Turbulent Viscosity |
| $P$ | Power |
| $f$ | Frequency |
| $M$ | Torque |
| $c_d$ | Drag coefficient |
| $c_l$ | Lift coefficient |

# Contents

# List of Figures

# List of Tables

# 1
# Introduction

Henry Ford once famously said "Any customer can have a car painted any color that he wants, so long as it's black". This quote is exemplatory for the early automotive industry. Compared to the modern automotive industry, there is a stark trend towards highly individual products. To meet the demand of the customers, the automotive industry is shifting to more agile and efficient engineering methodologies. One shift, wich can be observed is the transition from traditional full-scale wind tunnel testing to scale-model wind tunnel testing and computational fluid dynamics (CFD) simulations. However, the validation of such simulations still relies on physical testing, therefore it is crucial to be able to have a controlled test environment. However, wind tunnels are not able to reproduce the real world driving scenarios, which are inherently turbulent and unsteady. In order to test those scenarios in the wind tunnel, turbulence needs to be introduced in a controlled way. This can be achieved by active and passive turbulence generators.
Passive turbulence generators are stationary devices which are placed in the flow. They produce a predictable and steady level of turbulence. Active turbulence generators use moving elements which are powered by actuators to generate controllable turbulence. This method enables more complex and unsteady turbulence conditions. This leads to the need for active turbulence generation, since passive methods don't fulfill the desired criteria.

## 1.1 Aim

The Aim of this thesis is the development of an active turbulence generator for the Chalmers scale wind tunnel which can generate controlled turbulence intensities and frequencies which are found in real-world Vehicle Testing. Experimental Data shows that at highway speeds the turbulence intensity ranges between 1-5% [2], while urban driving scenarios can reach turbulence intensity levels between 5-15% [2].The turbulent lenght scale for real-world driving scenarios varies between 1-5m, which has to be taken into account while designing the components. This work can therefore be divided into several different tasks:

- Comparison of the amount and shape of airfoils needed to generate a homogeneous turbulence distribution across the entire test section with the desired turbulence intensity and turbulent length scales based on CFD Simulations.
- Simulation of aerodynamic forces and moment of inertia to calculate the power which the actuators need to supply
- Designing a mechanism which is able to convert the calculated power from

rotational motion into oscillating motion.
- Validation of the developed turbulence generator by measuring drag coefficients in the wind tunnel and comparing it to the simulation results.

# 2
# Theory

In this Chapter, the theoretical aspects related to turbulence, the motivation for using active turbulence generators, and the fundamentals of Computational Fluid Dynamics (CFD) are discussed. It also includes how turbulence is modelled in CFD tools and the role of wind tunnels in aerodynamic testing, including insights into the Chalmers wind tunnel. Furthermore, key differences between CFD and wind tunnel testing are highlighted.

## 2.1 What is turbulence?

"Turbulence is an irregular motion which in general makes its appearance in fluids, gaseous or liquid, when they flow past solid surfaces or even when neighboring streams same fluid past or over one another."
This is a definition of turbulence given by T. von Karman in 1937 who is known for his contributions to Fluid Dynamics. However, to fully understand what turbulence is, it is necessary to analyze how the flow can be categorized and what the main differences between these categories are.[5]

### 2.1.1 Laminar vs turbulent flow

Flow can be divided into two different states; the laminar flow and the turbulent flow. When the fluid is in a laminar state, it exhibits a smooth behavior and can be visualized as flowing in layers. In contrast, if the flow displays vortex-like behavior with many swirls, it is referred to as turbulent flow. Researchers also describe this as eddying motion or turbulent eddies. [23]

The Reynolds number (Re) is used to determine whether a flow is laminar or turbulent. Equation 2.1 shows that the Reynolds number is calculated based on the fluid density $\rho$, velocity $v$ and characteristic length $l$ divided by the dynamic viscosity $\mu$ of the fluid.

$$Re = \frac{\rho \cdot v \cdot L}{\mu} \tag{2.1}$$

The transition from a laminar flow to a turbulent flow occurs at a critical Reynolds Number $Re_{crit}$. For external flows, $Re_{crit}$ is $\geq 500000$ for streamlined bodies, while

around obstacles or bluff bodies, $Re_{crit}$ is $\geq$ 20000. In internal flows, the critical Reynolds number is $\geq$ 2300. Although these estimates provide useful guidelines, the exact critical values can vary depending on factors such as body shape, free-stream turbulence, surface conditions, blowing, suction, roughness, and other disturbances.[5]

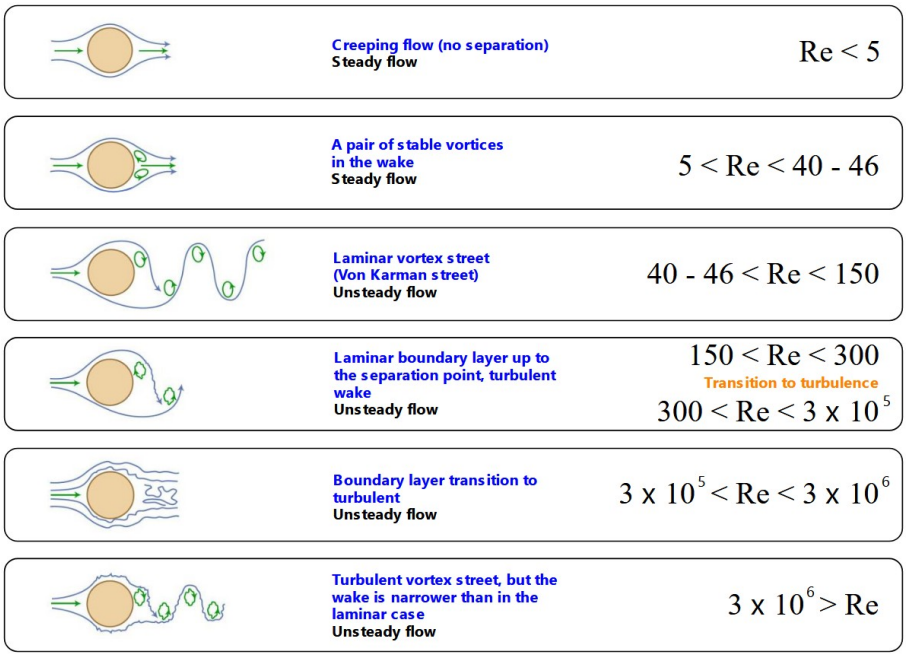


**Figure 2.1:** Flow state on cylinder on different Re numbers [5]

Figure 2.1 shows the transition from laminar to turbulent flow as the Reynolds number increases. The eddies visible behind the cylinder have different energy levels, which can be described using Kolmogorov's cascade.

A physical approach to describing turbulent flows involves Richardson's eddy hypothesis and Kolmogorov's spectrum. Richardson's hypothesis explains the dissipative behavior of turbulent flows, stating that large eddies, which carry significant energy, break down into smaller eddies with less energy. However, this hypothesis does not specify the scale of the smallest eddies. Kolmogorov addressed this by stating that the eddies continue to break down until they reach the Kolmogorov length scale ($\eta$). Beyond this point, the eddies will no longer break down further but instead dissipate their kinetic energy into heat. $\eta$ is defined as:

$$\eta = \left(\frac{\nu^3}{\epsilon}\right)^{\frac{1}{4}} \tag{2.2}$$

Here, $\nu$ is the kinematic viscosity of the fluid and $\epsilon$ describes the average dissipation rate of kinetic energy which is given by:

$$\epsilon = -\frac{\partial k}{\partial t} \tag{2.3}$$

There is also a relationship between the largest eddies ($l_0$) and the smallest eddies:

$$\frac{l_0}{\eta} \sim Re_T^{3/4} \tag{2.4}$$

with the turbulent Reynolds number $Re_T$ defined as:

$$Re_T = \frac{\kappa^{1/2} l_0}{\nu} \tag{2.5}$$

Here, $\kappa$ represents the turbulent kinetic energy.

Figure 2.2 shows the Kolmogorov spectrum.
In this Figure, the energy spectrum $\hat{E}$ is plotted over the wavenumber $\kappa$ of the turbulent eddies. It can be observed that as $\kappa$ increases, the eddy size $L$ decreases, following the relationship $\kappa \sim 1/L$. The energy cascade can be divided into three regions:

- **Energy containing range:** This range includes the largest eddies, which have small wavenumbers and contain the most energy.
- **Inertial range:** This is described by the relation $\hat{E} \sim \kappa^{-5/3}$. In this range, both the energy content and eddy size decrease proportionally.
- **Dissipation range:** Characterized by Kolmogorov length scale $\eta$, where viscous effects dominate and are responsible for the dissipation of energy into heat.

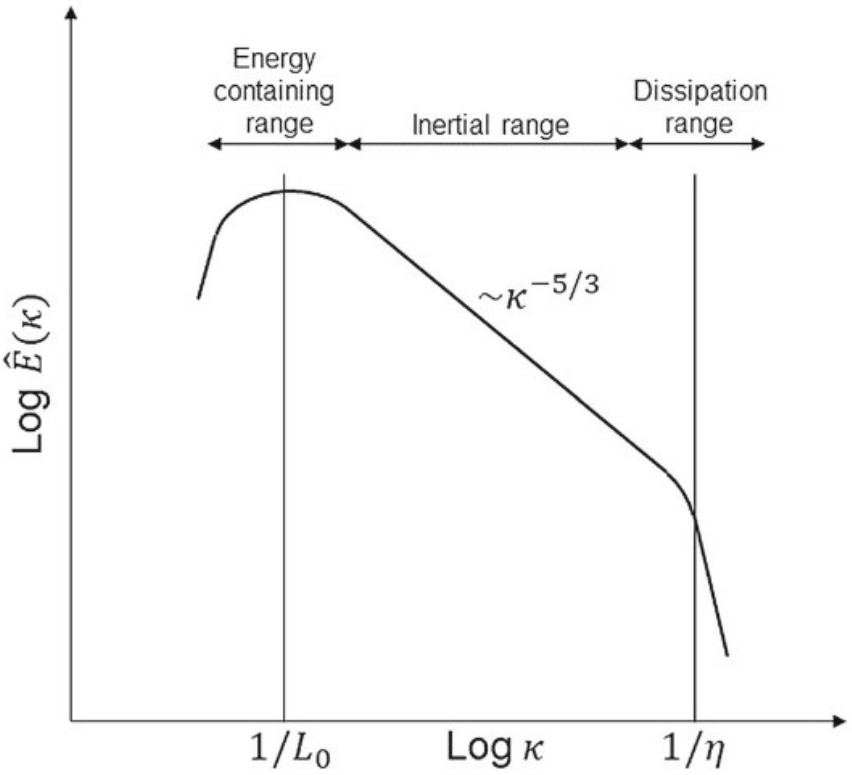


**Figure 2.2:** Kolmogorov Spectrum [9]

Turbulent flows can be observed in everyday life, such as rivers, smoke rising from chimneys, or even in cyclones in the atmosphere. They also depend on the flow velocity relative to the impacting object as well as the shape and surface characteristics of these objects. It is important to note that turbulent flows are highly unsteady and three-dimensional, as the instantaneous field fluctuates rapidly in all three directions, even if the time-averaged velocity shows components only in two coordinates. [3] [6] [12]

### 2.1.2 Turbulent length scale and turbulence intensity

The turbulent length scale and the turbulence intensity are two characteristic parameters used to determine the strength of the turbulence in that specific domain. As this thesis relies on these two parameters, they will be briefly introduced in the following sections.

#### 2.1.2.1 Turbulent length scale

The turbulent length scale defines the size of the dominant eddies within the flow. Referring back to Figure 2.2, the turbulent length scale corresponds to the left side of the spectrum, as it represents the size of the energy-containing eddies that govern the large-scale structures of the flow. The formula for calculating the turbulent length scale varies depending on the used turbulence model, and therefore, the corresponding expressions for the $\kappa - \epsilon$ and $\kappa - \omega$-SST models are provided in

Sections 2.2.3.4 and 2.2.3.5, respectively.

#### 2.1.2.2 Turbulence intensity

The turbulence intensity shows how chaotic and turbulent the flow is. In the context of real-driving scenarios, the turbulence intensity refers to the standard deviation in the velocity components normalized by the mean velocity of the vehicle. The turbulence intensity is evaluated as: [1] [2]:

$$I = \frac{u'}{U} \tag{2.6}$$

Where $u'$ is the root mean square of the turbulent velocity while $U$ is the mean velocity.

$$u' \equiv= \sqrt{\frac{1}{3}(u_x'^2 + u_y'^2 + u_z'^2)} \tag{2.7}$$

If the turbulent kinetic energy $\kappa$ is known, the root mean square can also be calculated as:

$$u' = \sqrt{\frac{2}{3}\kappa} \tag{2.8}$$

While the mean velocity is calculated as

$$U \equiv \sqrt{U_x^2 + U_y^2 + U_z^2} \tag{2.9}$$

## 2.2 What is CFD?

CFD stands for Computational fluid dynamics, which is used to simulate fluid flows in various environments and applications such as Aerodynamics or Thermodynamics. To understand how CFD works and which models are employed in this field, it is necessary to begin with its fundamental governing equations.

### 2.2.1 Governing equations

CFD is based on the governing equations of fluid flow, known as the Navier-Stokes equations. These equations rely on the control volume concept and are derived from the conservation principles of mass, momentum and energy. These equations are described as follows:

$$\text{Continuity} \quad \frac{\partial p}{\partial t} + div(\rho \mathbf{u}) = 0 \tag{2.10}$$

$$\text{x-momentum} \quad \frac{\partial pu}{\partial t} + div(\rho u \mathbf{u}) = -\frac{\partial p}{\partial x} + div(\mu grad(u) + S_{Mx} \tag{2.11}$$

$$\text{y-momentum} \quad \frac{\partial pv}{\partial t} + div(\rho v \mathbf{u}) = -\frac{\partial p}{\partial y} + div(\mu grad(v) + S_{My} \tag{2.12}$$

$$\text{z-momentum} \quad \frac{\partial pw}{\partial t} + div(\rho w \mathbf{u}) = -\frac{\partial p}{\partial z} + div(\mu grad(w) + S_{Mz} \tag{2.13}$$

$$\text{Energy} \quad \frac{\partial pi}{\partial t} + div(\rho i \mathbf{u}) = -pdiv(\mathbf{u}) + div(\kappa grad(T) + \Phi + S_i \tag{2.14}$$

$$\text{Equations of state} \quad p = p(\rho, T) \quad \text{and} \quad i = i(\rho, T) \tag{2.15}$$

$$\text{e.g. perfect gas} \quad p = \rho RT \quad \text{and} \quad i = C_v T \tag{2.16}$$

where the following mathematical operators are defined as:

$$grad(\phi) = \nabla\phi = \frac{\partial \phi}{\partial x}\hat{x} + \frac{\partial \phi}{\partial y}\hat{y} + \frac{\partial \phi}{\partial z}\hat{z} \tag{2.17}$$

$$div(F) = \nabla \cdot F\left(\frac{\partial}{\partial x}, \frac{\partial}{\partial y}, \frac{\partial}{\partial z}\right) \tag{2.18}$$

$$\begin{aligned} div(\mu grad(\phi) &= div\left(\mu\frac{\partial \phi}{\partial x}\hat{x} + \mu\frac{\partial \phi}{\partial y}\hat{y} + \mu\frac{\partial \phi}{\partial z}\hat{z}\right) = \\ &= \frac{\partial}{\partial x}\left(\mu\frac{\partial \phi}{\partial x}\right) + \frac{\partial}{\partial y}\left(\mu\frac{\partial \phi}{\partial y}\right) + \frac{\partial}{\partial z}\left(\mu\frac{\partial \phi}{\partial z}\right) \end{aligned} \tag{2.19}$$

These governing equations are discretized and the control volume concept must be applied. A control volume is an infinitesimally small element representing a finite region of the flow domain where the conservation laws of mass, momentum, and energy are applied in integral form. Evaluating the fluxes of fluid properties across the boundaries of each control volume transforms the continuous partial differential equations into a set of discrete algebraic equations that can be solved numerically. Figure 2.3 illustrates the concept of the control volume.

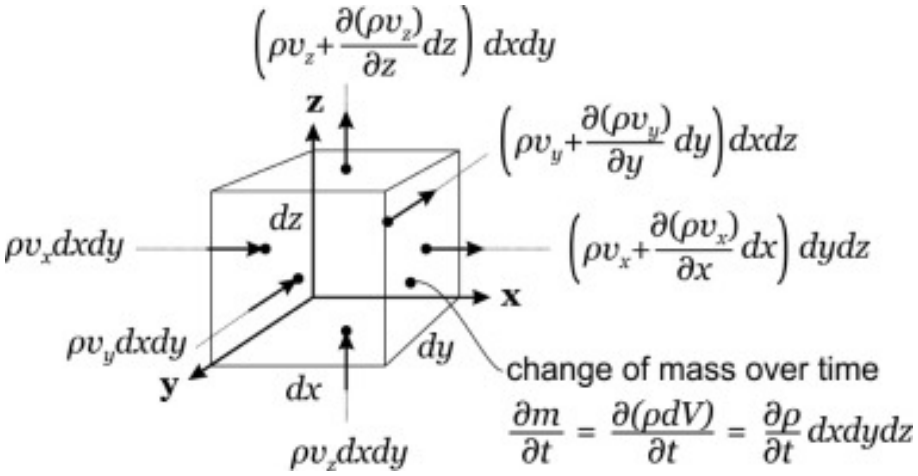


**Figure 2.3:** Infinitesimal control volume [17]

### 2.2.2 Boundary conditions

A computational domain requires the specification of boundary conditions to define the behaviour of flow at its limits, such as inflow, outflow, or interactions with solid surfaces. The two main types of boundary conditions are Dirichlet and Neumann conditions:

- **Dirichlet boundary conditions:** This is specified by the user and typically includes prescribed velocities, pressures, or temperatures based on prior measurements or derived values. These values can be set as constant or variable.
- **Neumann boundary condition:** This is a numerical boundary condition that links the boundary with the interior flow field. The values are computed by the program rather that set directly. Neumann conditions are most accurate when derived directly from the governing equations, as they correctly represent the underlying physics. However, if these values are determined by simple extrapolation of interior field variables to the boundaries, the accuracy of the solution may decrease.

[11] [15]

### 2.2.3 Turbulence modeling in CFD

In CFD, three major approaches are used to model turbulence: Direct Numerical Simulation (DNS), Large Eddy Simulation (LES), and Reynolds-Averaged Navier–Stokes (RANS). This thesis will briefly describe DNS and LES but will focus primarily on RANS, as the simulations in this work are based on RANS models. Figure 2.4 illustrates these models in a pyramid. In addition to DNS, LES, and RANS, hybrid RANS–LES models also exist, combining both approaches within one domain to achieve improved accuracy with lower computational costs compared to a full LES.

#### 2.2.3.1 DNS

Direct Numerical Simulation (DNS) is the most computationally intensive turbulence model that can be used in CFD. It provides the most precise solutions, as it

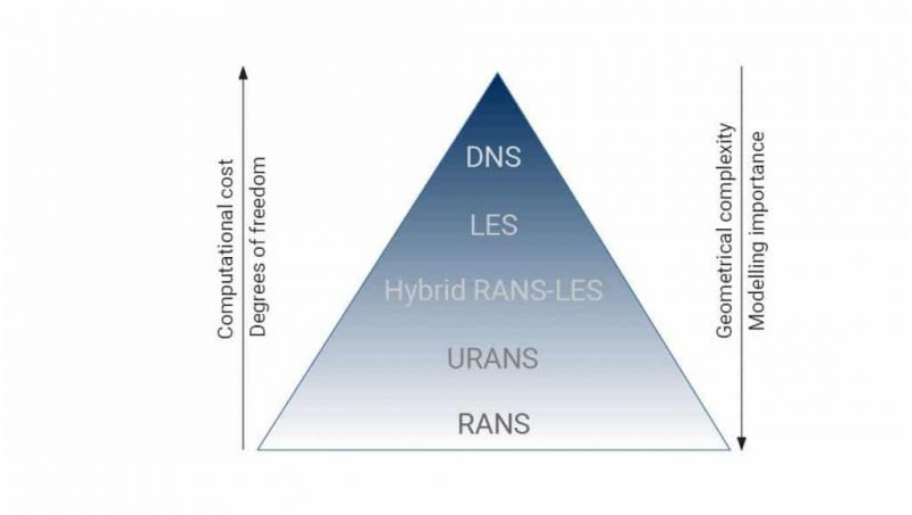


**Figure 2.4:** Turbulence models in CFD [8]

solves the Navier-Stokes equations directly without using any kind of approximations. This enables highly accurate predictions of velocities, pressures, and other flow variables. DNS requires extremely fine meshes to resolve all turbulent scales, which leads on high demanding resources. Due to this high computational cost, DNS is currently limited to simple and easy domains. Despite its accuracy, the resource demands of DNS make it impractical for most industrial applications and is predominantly used in research. These simulations are often used to better understand the mechanism of turbulence generation, heat transfer, and dissipation in turbulent flows, as well as to simulate aerodynamic noise or to investigate the effects of compressibility on turbulence, among many other applications. Figure 2.5, shows the accuracy of DNS. The upper part of the picture corresponds to the experiment that is performed, while the lower part shows the DNS simulation. [3] [10]

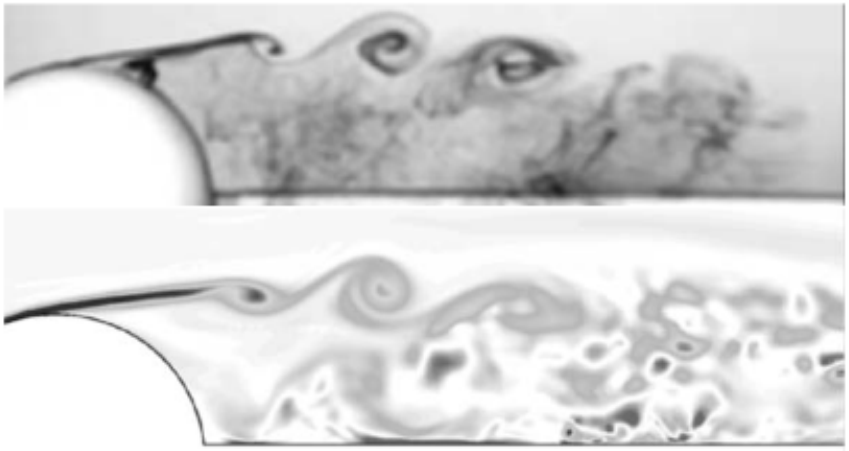

**Figure 2.5:** Comparison between experiment(top) and DNS simulation(bottom) [3]

#### 2.2.3.2 LES

Large Eddie Simulation (LES) directly resolves the larger turbulent eddies from the governing equations, similar to DNS, while modelling the smaller eddies through a Subgrid Scale (SGS) model. The most widely used SGS model is the Smagorinsky-Lilly-Model, which is based on the Boussinesq-Hypothesis so that it can calculate the fine eddies. Figure 2.6 shows a comparison between experimental data ( Figure 2.6 (a)) and LES results ( Figure 2.6 (b)), highlighting how LES captures the larger eddies that are larger than the grid spacing, while filtering out the smaller eddies. [3] [4]

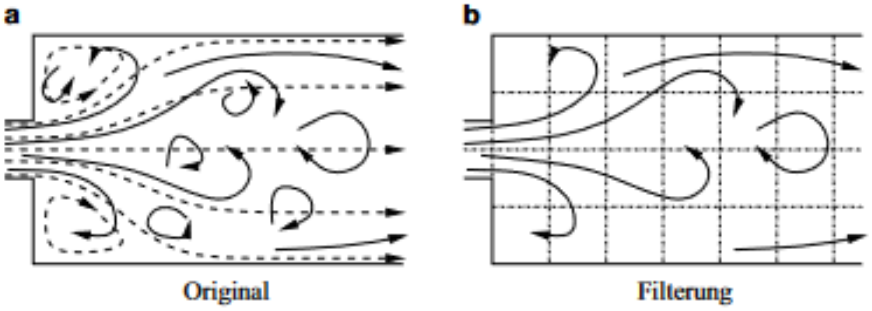


**Figure 2.6:** LES filtering [20]

#### 2.2.3.3 RANS

RANS stands for Reynolds-Averaged Navier-Stokes, an approach that provides time-averaged solutions of the flow and turbulence quantities. RANS models are well-suited for industrial simulations due to their relatively low computational cost. Figure 2.7 explains the concept of RANS modelling. In Figure 2.7a, turbulence is shown with vortices of various sizes from an experimental perspective, whereas Figure 2.7b, demonstrates how RANS models these turbulent effects via Reynolds averaging to produce the mean flow field.

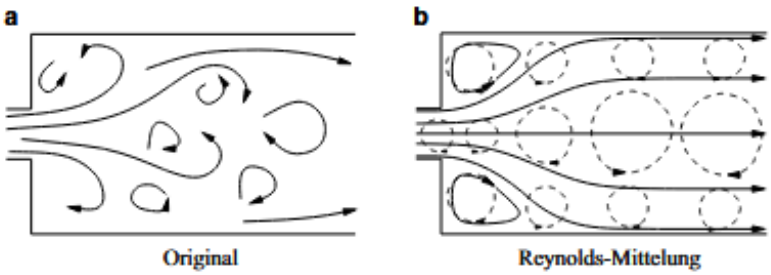


**Figure 2.7:** RANS averaged flow [20]

This averaged flow field is calculated using the Reynolds averaging formula. In this case, the flow quantity $\phi$ is decomposed into a time-averaged component $\bar{\phi}$ and a fluctuating component $\phi'$:

$$\phi = \bar{\phi} + \phi'(t) \tag{2.20}$$

#### 2.2.3.4 $\kappa - \epsilon$

The $\kappa - \epsilon$-model is one of the most widely used RANS turbulence models and is considered the standard two-equation model. This model is well suited for flow calculations within the domain and is also frequently used for global flow structures where detailed local accuracy is not critical. However, this model is unsuitable for flows that separate from the wall due to the pressure gradients. Since the separation is calculated too late and the separation region is too small. The $\kappa-\epsilon$-model also has the limitation that it does not support low Reynolds wall treatment and therefore requires using the high Reynolds wall treatments. (Wall treatment methods will be discussed later in this Chapter.)
In the $\kappa - \epsilon$-model, the turbulent length scale $l_t$ is typically estimated using:

$$l_t = \frac{\kappa^{3/2}}{\epsilon} \tag{2.21}$$

where $\kappa$ is the turbulent kinetic energy and $\epsilon$ is the dissipation rate. This formulation provides an estimate of the characteristic size of the energy-containing eddies in the flow.[7] [11] [20]

#### 2.2.3.5 $\kappa - \omega$-SST

This the $\kappa-\omega$-SST-model ihas gained increasing importance in CFD as it combines the advantages of the $\kappa-\epsilon$ and the $\kappa-\omega$-models. While the $\kappa-\epsilon$-model performs well in free-stream regions, the $\kappa - \omega$-model is more accurate in near-wall regions. The $\kappa-\omega$-SST-model combines both models to achieve optimal performance throughout the domain. It also incorporates a modified eddy-viscosity formulation to limit pressure-induced stresses in regions of rising pressure.
For the $\kappa - \omega$-SST-model, the turbulent length scale is often approximated by:

$$l = \frac{\sqrt{\kappa}}{0.09 * \omega} \tag{2.22}$$

where $\omega$ is the specific dissipation rate[4] [20] [11]

## 2.3 Wall treatment

In turbulence modeling the near-wall region is of major importance, as the velocity decreases towards the wall and the velocity gradients increases. This is due to the fact that the walls have a no-slip condition, combined with the significant decrease in turbulence near the wall and the drastic increase in viscous friction effects. Additionally, cross-flow movements are suppressed in this region. Figure 2.8 shows a

comparison of the velocity profiles in a pipe between a laminar and a turbulent flow, illustrating that the velocity gradient is greater in turbulent flows.

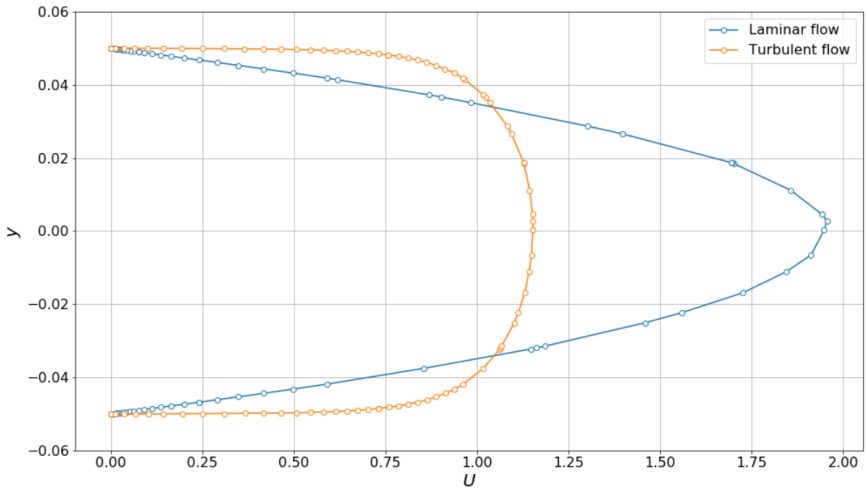


**Figure 2.8:** Comparison of laminar and turbulent velocity profiles in a pipe [7]

To resolve these gradients, the transition from the wall to the core flow (known as the boundary layer) must be modeled. Two main approaches can be used:

- The first approach involves fully resolving the near-wall boundary layer using Low Reynolds Number (LRN) models, which require a very fine mesh to fully capture the gradients.
- The second approach is the High Reynolds Number (HRN) method, which avoids full resolution of the flow up to the wall by modeling the near-wall region using non-linear wall functions.

[6] [12] [20]

Figure 2.9 illustrates the meshes used for each approach. The LRN mesh on the left demonstrates the fine resolution required to capture the boundary layer, whereas the HRN mesh on the right uses a coarser grid and applies a wall function to accurately model near-wall behavior.

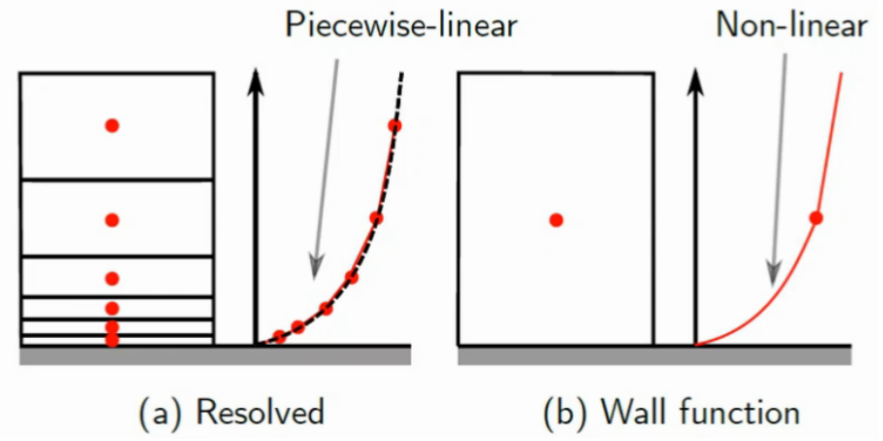


**Figure 2.9:** LRN (left), HRN (right) [22]

### 2.3.1 High-Re Models with Wall Functions

To resolve the boundary layer and its gradients, a very fine mesh is required. However, in practice, this significantly increases computational demand. Therefore, wall functions have been developed to bridge the viscous sub-layer using empirical wall laws.

Through extensive experimental observations, the mathematician Theodore von Kármán noted that the velocity near the wall exhibits a universal character. Based on these observations, he derived a universal wall law (Law of the Wall) from the averaged momentum equations to represent the near-wall behavior of turbulent flows. This law is based on non-dimensionalising the velocity ($u$) and the wall distance ($y$). The dimensionless velocity ($u^+$) and the dimensionless wall distance ($y^+$) are defined as follows:

$$u^+ = \frac{u}{u_\tau} \qquad y^+ = \frac{y u_\tau}{\nu} \tag{2.23}$$

Here, $u_\tau$ is the friction velocity, defined as:

$$u_\tau = \sqrt{\frac{\tau_w}{\rho}} \tag{2.24}$$

The wall shear stress $\tau_w$ can be derived from the velocity gradient using:

$$\tau_w = \mu \frac{\partial u}{\partial y} \tag{2.25}$$

This wall law can be applied to universal flow profiles. The dimensionless wall distance ($y^+$) is divided into three regions, as shown in Figure 2.10. Note that the X-axis is scaled logarithmically, and the black line represents the "correct" line obtained from DNS simulation and experimental data.

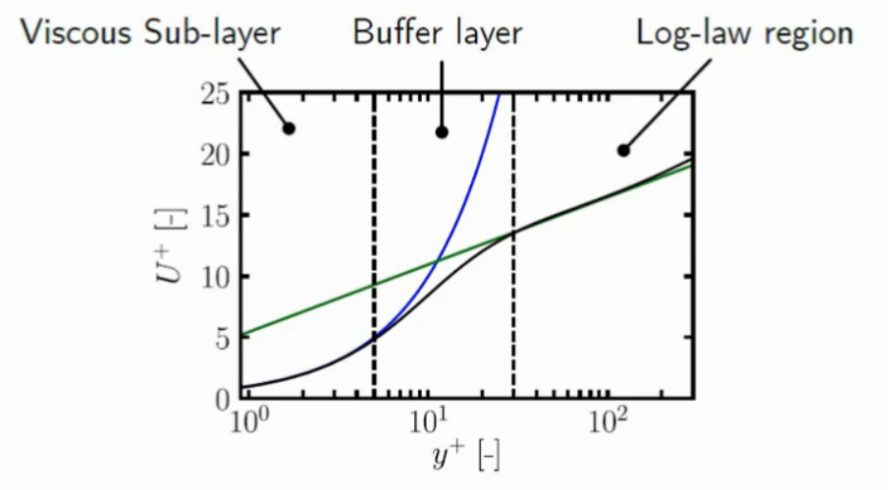


**Figure 2.10:** Universal wall law [22]

The first region, the viscous sub-layer, lies in the range of $0 < y^+ < 5$. At $30 < y^+ < 300$, the log-law can be observed, and between these two ranges the buffer layer exists. In the viscous sub-layer, turbulence effects are neglected, resulting in a linear relationship between $u^+$ and $y^+$. This is represented as follows:

$$u^+ = y^+ \tag{2.26}$$

In the log-law region, where viscous effects are lower, the dimensionless velocity is given by:

$$u^+ = \frac{1}{\kappa} ln(y^+) + C \tag{2.27}$$

Here, $\kappa \approx 0,41$ is the von Kármán constant and $C \approx 5,0$ is an integration constant. Neither of these two equations describes the intermediate buffer layer accurately. Therefore, CFD codes combine both wall functions. Since both equations intersect at $y^+ \approx 11.25$, the linear function is used below this value, while the logarithmic formulation is used for values above. For HRN approaches, it is recommended to maintain $y^+ > 20$, although the values in the literature vary between 20 and 30. [12] [20] [22]
Turbulent flow variables such as $\kappa, \omega, \epsilon, \nu_t,$, etc., also exhibit universal characteristics similar to the velocity $u$. These are also non-dimensionalized and gain general applicability:

$$\kappa^+ = \frac{\kappa}{u_\tau^2} \qquad \omega^+ = \frac{\omega\nu}{u_\tau^2} \qquad \epsilon^+ = \epsilon\frac{\nu}{u_\tau^4} \qquad \nu_t^+ = \nu_t\frac{\epsilon}{\kappa^2} \tag{2.28}$$

These quantities can be integrated into turbulence models. However, their detailed implementation is not further discussed in this work.
High-Re models with wall functions are commonly used, as they significantly reduce computation time by avoiding the need for fine near-wall meshes. Nevertheless, it is important to note that these wall functions are based on empirically derived equations, meaning their range of validity must be considered. [12] [20]

### 2.3.2 Low-Re Models

Unlike High-Re models, Low-Re models do not use wall functions but resolve the flow all the way to the wall. To accurately capture the transition from the fully turbulent core flow to the boundary layer and the wall, damping functions are applied to turbulence quantities. These functions are introduced and modified in models such as $\kappa - \epsilon$-model. They damp the dissipation rate $\epsilon$ near the wall and the turbulent viscosity $\mu_t$ in each mesh cell.
To ensure proper functioning of the Low-Re model, a $y^+$ value below 1 is required. The two damping functions are defined as:

$$f_\epsilon = (1 - 0,3e^{-Re_\tau^2}) \tag{2.29}$$

$$f_\mu = e^{-\frac{3,4}{1+0,02Re_\tau^2}} \tag{2.30}$$

For detailed modifications to the transport equations, refer to [20].

When comparing the High-Re and Low-Re models, it cannot be universally stated that one approach is superior. While Low-Re models generally offer higher accuracy by avoiding the model errors associated with wall functions, they require significantly greater computational resources due to the fine mesh requirements and may also suffer from instabilities or reduced convergence rates. Therefore, the choice of modeling approach should be based on the specific characteristics and requirements of the flow problem under investigation.

## 2.4 What is a wind tunnel

A wind tunnel is used to obtain experimental measurements of how an object behaves under real-world flow conditions. Wind tunnels are applied in a wide range of scenarios, from studying the behavior of small objects such as balls up to conducting aeronautical experiments. Therefore, they can be found in various scales, depending on the intended application and available resources. However, the wind tunnel technology behind it remains the same, regardless of its size. Wind tunnels can be designed in two main configurations: The open return wind tunnel (Figure 2.11a) and the closed return wind tunnel (Figure 2.11b).

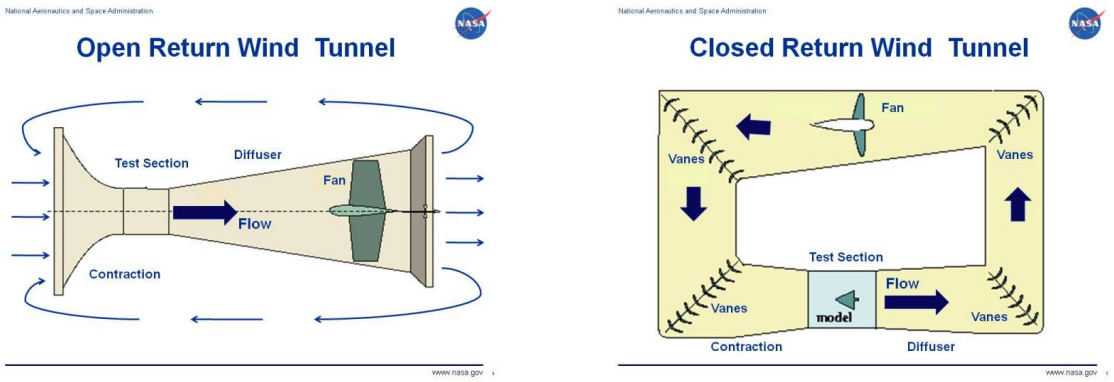


**(a)** Open return wind tunnel [14] **(b)** Closed return wind tunnel [13]

**Figure 2.11:** Wind tunnel configurations

The open return wind tunnel allows air to flow in from external environment and exhausts it back into the surroundings. The closed return wind tunnel consists of a closed-loop system in which the air is recirculated. This approach maintains more stable air properties and increases energy efficiency.
Despite one tunnel being open and the other closed, both configurations share similar components. Both include a wind tunnel fan, a diffuser, and a test section.

The test section of a wind tunnel can also have different wall configurations. These are chosen based on the type of test that must be performed in the tunnel. Figure 2.12 illustrates the possible configurations found in wind tunnels worldwide,

including open, closed, slotted, streamlined, and adaptive walls.

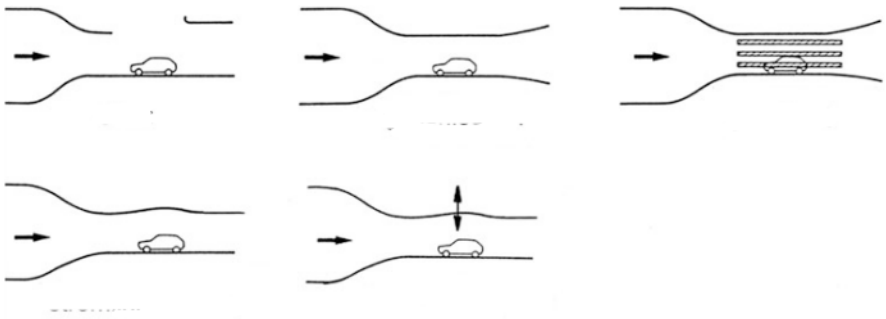

**Figure 2.12:** Different wall configurations [19]

## 2.5 Differences between CFD and the Wind tunnel

CFD and wind tunnel testing are essential tools for the analysis and optimization of flow behavior around objects in the field of aerodynamics and fluid mechanics. Although both aim to predict aerodynamic performance, their methodologies differ fundamentally.
One key distinction lies in the environment of operation. CFD operates in a virtual environment, while wind tunnel testing requires physical prototypes. Since CFD operates in virtual environments, it can be used for rapid iterations and design modification without the need for manufacturing physical components. In contrast, wind tunnel testing requires a physical model and allows researchers to observe real-world interaction between the fluid and the object, which can reveal effects that are difficult to capture computationally.
From a financial standpoint, the CFD method is highly suitable for preliminary design studies and parametric analyses due to its lower cost and flexibility. However, when advanced simulation models such as LES or DNS are used, the computational demand and expertise required increase significantly. Wind tunnel testing has a higher cost demand due to model fabrication, facility operation, and instrumentation requirements. Additionally, time must be allocated for model preparation and experimental setup. Nevertheless, wind tunnel testing often yields highly reliable data.
In industrial applications, particularly in the aerospace and automotive sectors, wind tunnel testing is considered a benchmark for validation and is also a prerequisite for regulatory certification. CFD, on the other hand, is widely accepted as a design and optimization tool, but typically requires validation against experimental data to ensure confidence in critical decision-making processes.
In summary, CFD and wind tunnel testing are not competing approaches, but rather complementary methodologies. CFD delivers detailed insights at lower cost and high flexible design iterations, while wind tunnel testing offers high-fidelity, physically validated data essential for verification, validation, and certification. In modern

aerodynamic analysis and development, a hybrid approach that uses the strengths of both methods is often the most effective strategy.

## 2.6 Turbulence generators

If experiments are conducted in a wind tunnel without any additional obstacles, the experiments will run in a low turbulence environment, since the airflow in the test section remains highly laminar and, therefore, cannot get a high turbulence intensity. However, real-world scenarios involve vehicles being exposed to high levels of turbulence due to wind gusts, obstacles, or preceding vehicles. To replicate such conditions with greater accuracy, researchers utilize turbulence generators to increase turbulence intensity within the test section. There are two main types of turbulence generators in wind tunnels: Passive and active turbulence generators.
**Passive turbulence generators** operate by introducing static objects or shapes in front of the test section so that the flow is obstructed, increasing the turbulence in the wind tunnel. Figure 2.13 illustrates a passive turbulence generator mounted in the wind tunnel. Once installed, the passive generator remains fixed throughout the experiment, providing a constant level of turbulence intensity.

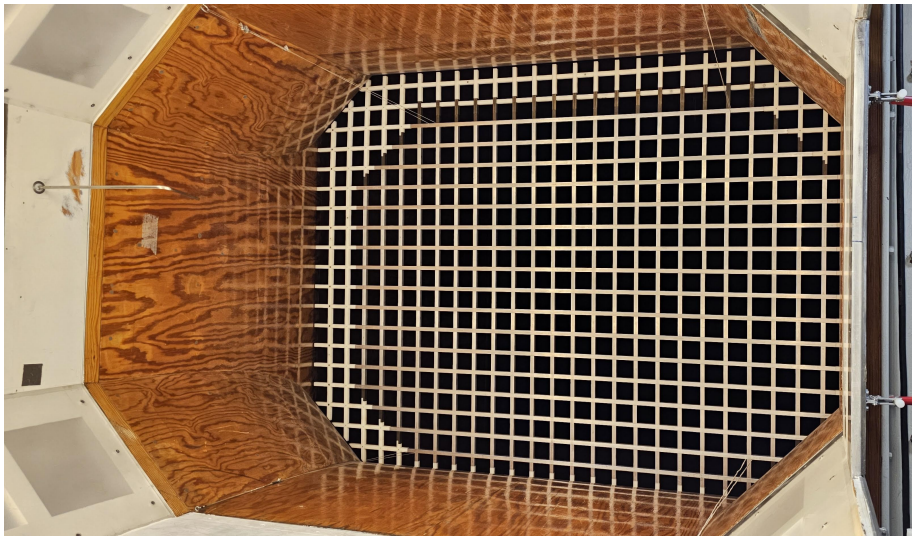

**Figure 2.13:** Passive turbulence generator

**Active turbulence generators**, in contrast, use active control mechanisms to increase the turbulence in the test section. Unlike passive generators, they consist of non-static components that can be mechanically actuated to modify the flow and achieve higher and adjustable turbulence intensities. Figure 2.14 shows the turbulence generator used in this study, which serves as an example of an active turbulence generator. It is inserted into the wind tunnel and actuated by mechanical devices to create variable turbulence conditions.

**Figure 2.14:** Active turbulence generator

Although active turbulence generators require additional energy input to operate their mechanical components in the wind tunnel, they offer significant advantages. While passive generators provide a fixed level of turbulence once installed, active generators enable controlled variation, allowing a reproduction of a wider range of real-world turbulence conditions within the wind tunnel.[24]

# 3

# Methods

In this Chapter the methods for developing a turbulence generator, which is able to reproduce the turbulence intensities and turbulent length scales that occur in real world driving scenarios within a controlled model scale wind tunnel will be discussed. The approach taken in this study combines CFD with mechanical design, prototyping and testing to validate the induced turbulence by measuring the drag coefficent on a drivAer model. The DrivAer model, developed by the Technical University of Munich (TUM), is a commonly used open-source reference geometry designed to bridge the gap between highly idealized aerodynamic shapes and complex production vehicles. It offers a realistic, yet standardized platform for aerodynamic investigations, making it highly valuable for validating computational fluid dynamics (CFD) methods and turbulence modeling strategies. The model includes the rear-end configurations of a fastback, estate, and notchback—allowing researchers to analyze the influence of geometry on flow separation, wake formation, and drag. In the context of this thesis, the notchback configuration of the DrivAer model is used to simulate realistic vehicle aerodynamics under controlled turbulent conditions, generated by an active turbulence generator. This setup enables the study of how upstream disturbances influence the wake of the vehicle and providing deeper insight into turbulence-vehicle interaction in automotive applications.

## 3.1 Physical model for CFD

In order to accurately asses the impact of the design parameters, which will be discussed later, an appropriate turbulence model has to be selected. Based on literature, the models k-$\epsilon$ and k-$\omega$ SST were identified as suitable models for the simulation of vehicle aerodynamics.

To evaluate the performace of the different turbulence models, steady-state simulations of the DrivAer model without induced turbulences were simulated within the wind tunnel. After conducting a mesh study for both models, the drag coefficients were compared to experimental data obtained by [18].

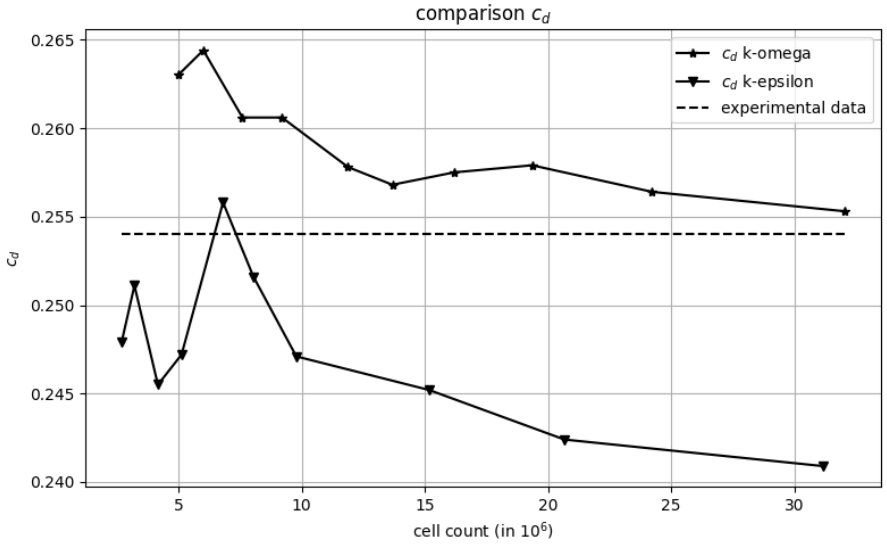


**Figure 3.1:** Comparison of drag coefficients from simulations and experiments.

By comparing the calculated values to the experimental data, k-$\omega$ SST has a better correlation. The deviation compared to the experimental data can be explained by the small differences between the physical and the computational model. The superiority in the simulations compared to k-$\epsilon$ is also consistent with the findings of [16]. The prism layers of the DrivAer Notchback configuration for the k-$\omega$ SST turbulence model were specified as followed:

| **Base size** | 5 mm |
|---|---|
| **Prism Layer controls** | |
| Number of Prism Layers | 12 |
| Near Wall Thickness | 6.25 $\mu$m |
| Total thickness | 3.25 mm |

**Table 3.1:** Mesh Settings

In order to capture the wake behind the vehicle under turbulent conditions, a wake refinement to the domain with the following values has been added:

| **wake refinements** | |
|---|---|
| Wake distance | 1.3m |
| Angle | 7deg |
| Default growth rate | slow |

**Table 3.2:** settings wake refinement

By applying those settings, the following mesh is created:

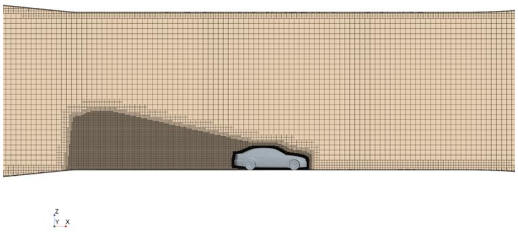

**Figure 3.2:** Wake refinement

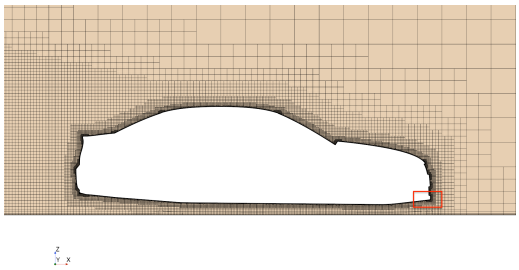

**Figure 3.3:** Vehicle refinement

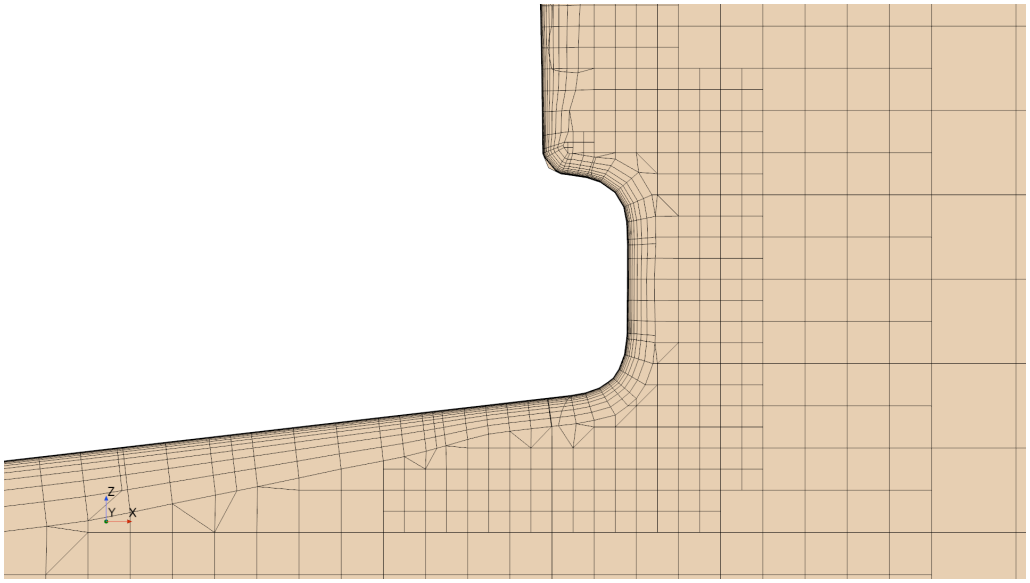


**Figure 3.4:** Prism layers

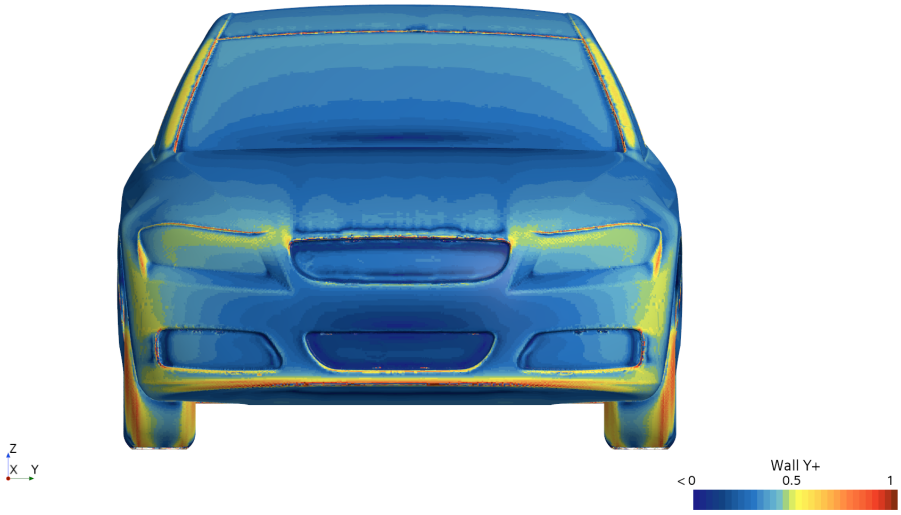


**Figure 3.5:** Front view y+


**Figure 3.6:** Rear view y+

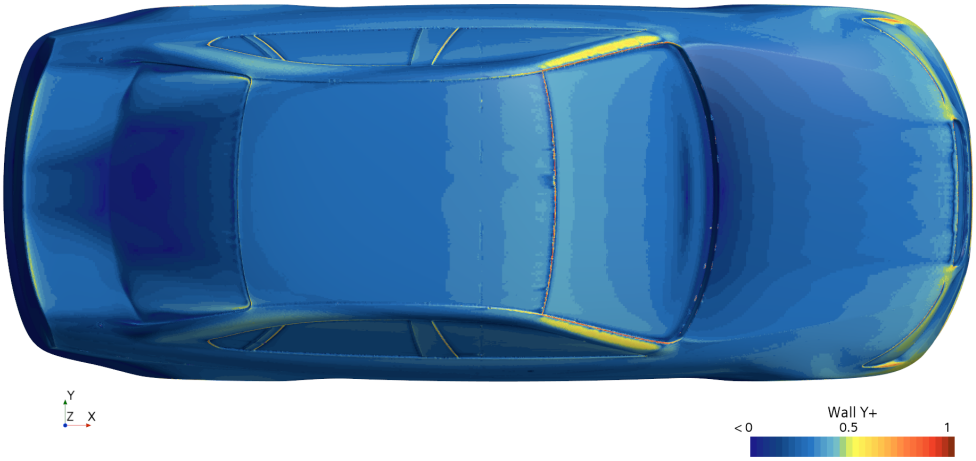


**Figure 3.7:** Top view y+

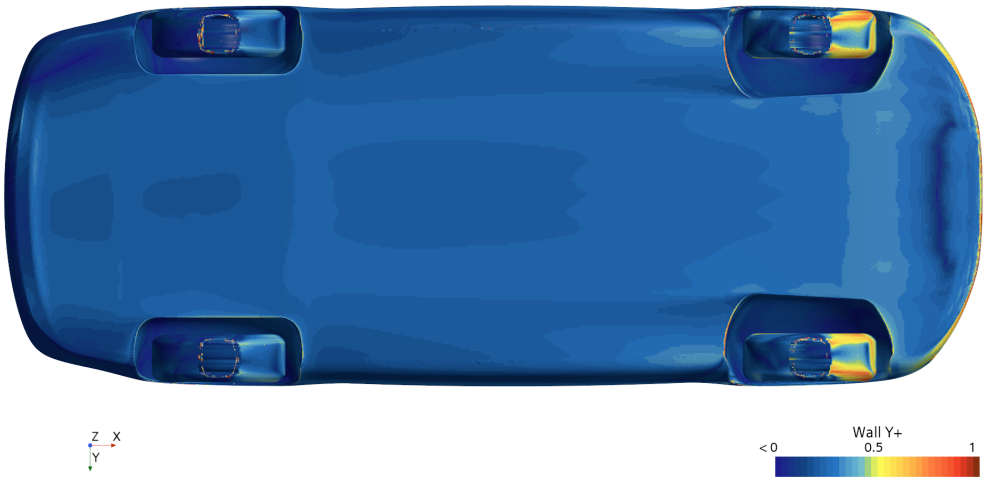


**Figure 3.8:** Bottom view y+

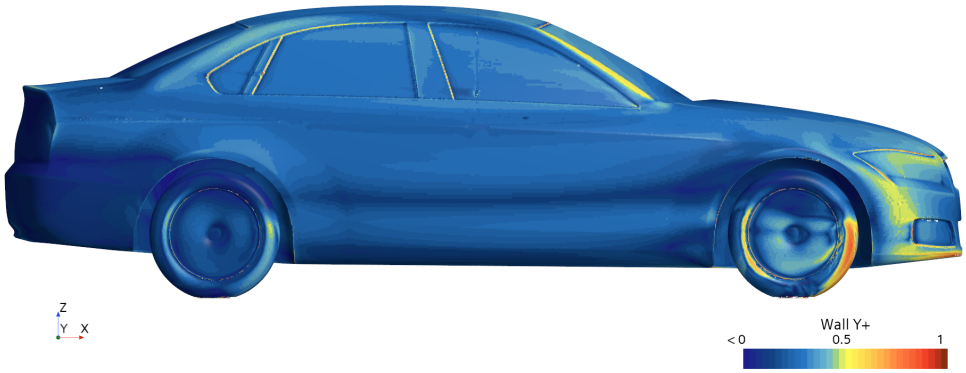


**Figure 3.9:** Side view y+

It can be seen that the y+ values are small enough to capture the viscous sublayer. This can be achieved with y+ values below 3. One could argue that the mesh is unnecessary fine, however turbulent flow will be simulated, which will lead to time-dependent values which will locally increase the y+ values.

## 3.2 Selected Airfoil

As method to induce controlled turbulence, movable wings were placed into the flow area. This method can be seen in the FKFS-Swing [21] as well. With the goal of a homogeneous turbulence intensity across the whole test section, seven wings were

placed in the flow. One performance-defining parameter is the Airfoil shape of the wings. A good source for Airfoil shapes is given by the National Advisory Committee for Aeronautics (NACA) which is the predecessor of the National Aeronautics and Space Administration (NASA). The NACA airfoil shapes are a family of mathematically defined profiles that are widely used in aerodynamic applications. These airfoils are categorized using a numerical code that describes specific geometrical properties, such as camber, thickness, and chord distribution. The NACA 4-digit series, to which the NACA 0015 belongs, is characterized by a simple yet effective design where the first digit indicates the maximum camber (0% for symmetric airfoils like the 0015), the second digit denotes the position of the maximum camber (also 0% for symmetric shapes), and the last two digits represent the maximum thickness as a percentage of the chord length (15% in this case).

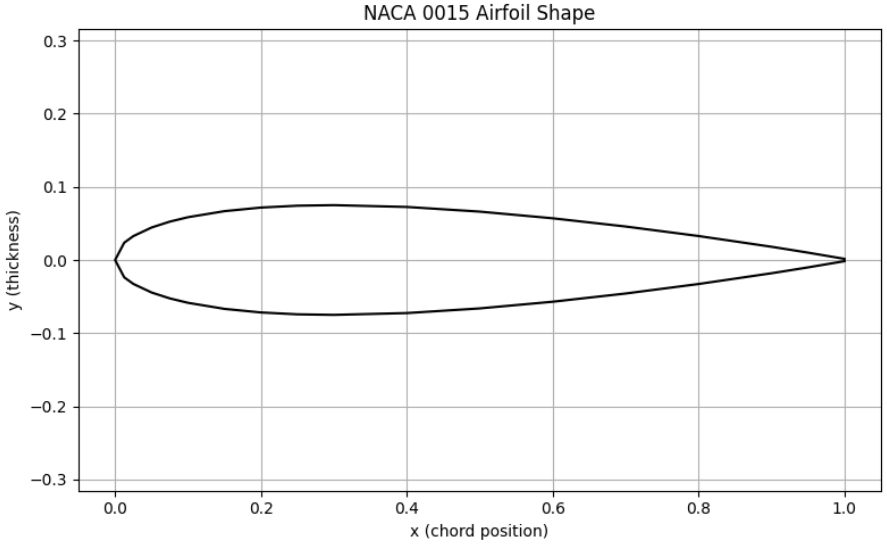


**Figure 3.10:** Airfoil shape.

The NACA 0015 is a symmetric airfoil without camber and a relatively moderate thickness, making it a popular choice for applications in which balanced aerodynamic performance is important. The symmetry of the airfoil ensures that it generates no lift at zero degrees of angle of attack, which is particularly advantageous in turbulence generation systems in which neutral aerodynamic behavior at baseline conditions is advantageous.

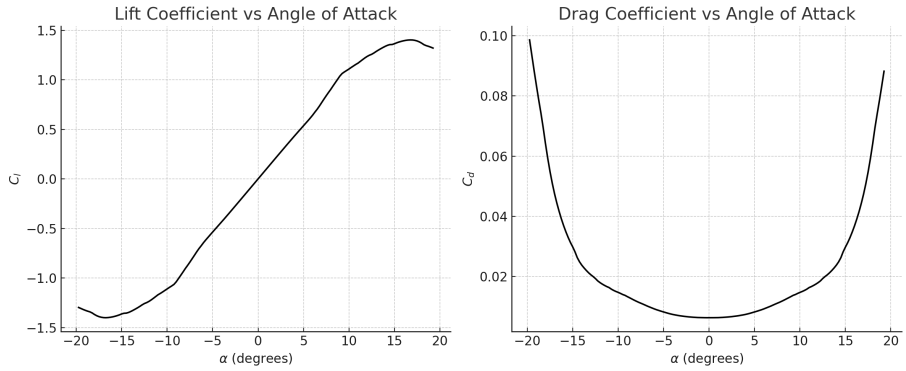


**Figure 3.11:** Characteristical coefficients of NACA 0015

With the physical model validated under steady-state conditions and the turbulence model proven to be appropriate, the next step involves preparing the simulation domain to be able to move the wings time dependent in order to be able to achieve unsteady behavior. Since the physical model has already been set, only grid convergence for the overset mesh regions needs to be analyzed. For this purpose, another mesh study has been done with wings angled at 20° which resulted in a base-size for the overset regions of 7.5mm. To realize an unsteady simulation with moving components, the overset mesh operation has been used. This operation in STAR-CCM+ is a robust and flexible technique used to model complex simulations involving moving or dynamically changing components. It works by allowing multiple different mesh regions to overlap within a domain, most commonly a stationary background mesh combined with one or more overset meshes that can translate, rotate, or deform independently. In this case setup the background mesh was made out of the volume inside the wind tunnel and seven overset mesh regions, one for each wing since each wing had it's own rotational axis. As a result, the overset mesh operation simplifies the handling of relative motion between parts and enhances the efficiency and versatility of simulations involving mechanical systems.
A key aspect of ensuring accuracy in overset mesh simulations is the quality of data transfer across the overlapping regions. Information such as velocity and pressure must be interpolated from the donor cells in one mesh to receptor cells in another. For this interpolation to be both accurate and numerically stable, it is highly beneficial that the overlaying cells in the background and overset meshes should have similar sizes. When cell sizes are well-matched, interpolation errors remain low.. Conversely, large discrepancies in cell size can lead to poor resolution of physical features and inaccuracies at the interface, potentially degrading the overall solution. Maintaining comparable cell sizes in overlapping regions is therefore essential for achieving high-quality results in overset mesh simulations. An example of this operation is visualized in figure 3.12 and figure 3.13.
In order to design the mechanism, loads must first be calculated. To do so, an unsteady simulation was conducted. All seven wings were rotated along the rotation axis for every timestep which represents 0.001 seconds in real time.
The result of this simulation gives us the following moments as shown in figure 3.14. The plot is the sum of the individual moments of each wing. The moment can be divided into the components of mass inertia and aerodynamic forces.

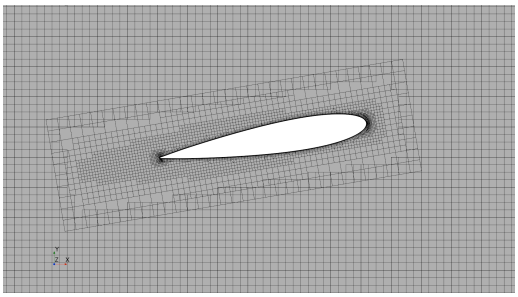

**Figure 3.12:** Initial overset mesh

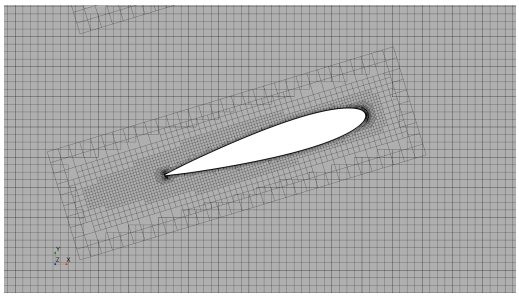

**Figure 3.13:** After 4 timesteps

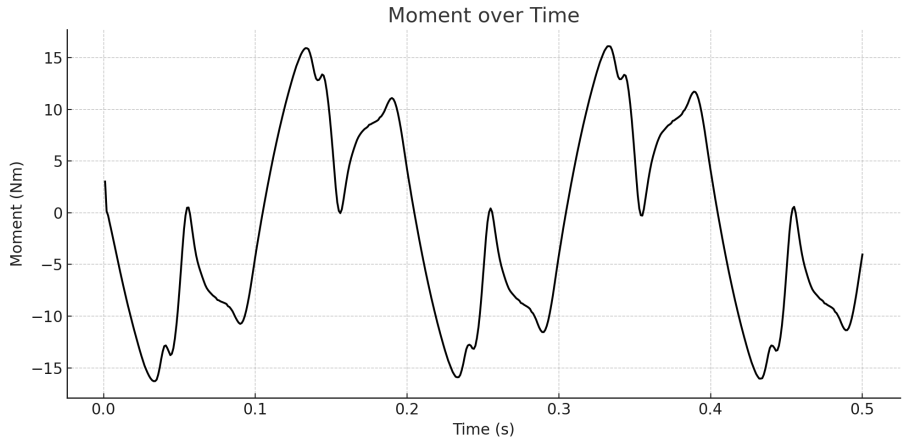


**Figure 3.14:** Plot of the summed moments over time

From the maximum Moment of 16Nm, the power needed for the drivetrain can be calculated with

$$P = 2\pi \cdot f \cdot M \tag{3.1}$$

The needed power can therefore be calculated as 502W. Based on the moments obtained from the CFD simulation, the mechanical design of the drive system can now be carried out.

## 3.3 Mechanical Design

To actuate the wings, a suitable mechanical system is required. The objective was to move all seven wings in phase, rather than controlling each motor individually. Therefore, a mechanism driven by a single motor with mechanical linkages connecting the wings was considered the most appropriate solution. This approach eliminates the need for complex synchronization through feedback loops. Additionally, it is necessary to convert the rotational motion of the electric motor into the oscillatory motion required for wing movement.

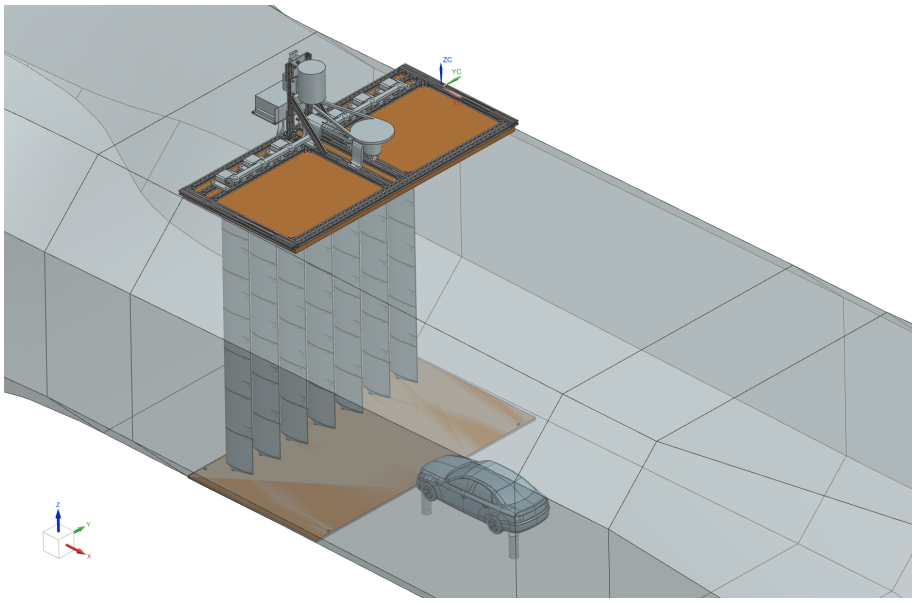

**Figure 3.15:** Isometric View of the entire Assembly with DrivAer Model and wind tunnel

The whole mechanical drivetrain is supported by an aluminum frame, which is made of 20mm x 20mm profiles. The two plates which can be seen in the images are made out of plywood. The upper plate is screwed into the aluminum profile and the bottom plate is screwed into the frame of the wind tunnel.

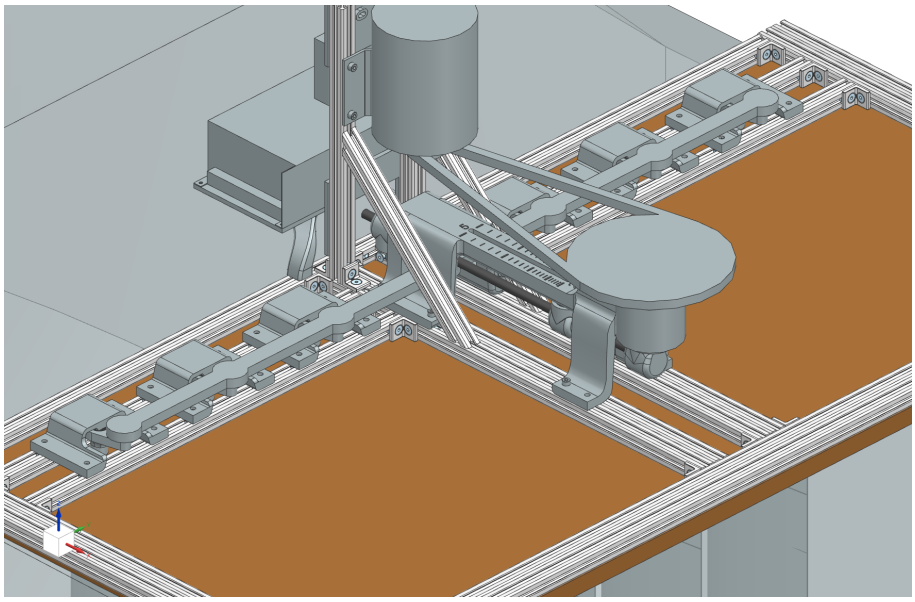

**Figure 3.16:** Close-up view of the mechanism

The black rod in Figure 3.16 is made out of carbon fiber. This decision was made due to the low weight, combined with high stiffness of the material. All of the remaining parts are designed to be 3D printed. This enabled rapid prototyping. Due to the high expected loads and the limited knowledge in FEM-Simulations, conser-

vative measures were taken to guarantee the structural integrity of the components. Settings of the print were:

| **print settings** | |
|---|---|
| material | PLA |
| wall layers | 6 |
| infill | 15% |
| infill type | gyroid |
| nozzle diameter | 0.4mm |
| layer height | slow |
| support structure | organic |

**Table 3.3:** settings print

The most important component of the whole mechanism is the mounting, which Transfers the full load of the motor. The bearings were mounted with a press-fit. In order to strengthen the connections, most of the pins holding the bearings were replaced by carbon rods.

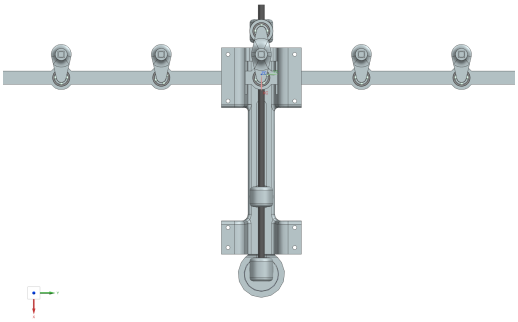

**Figure 3.17:** 0° rotation

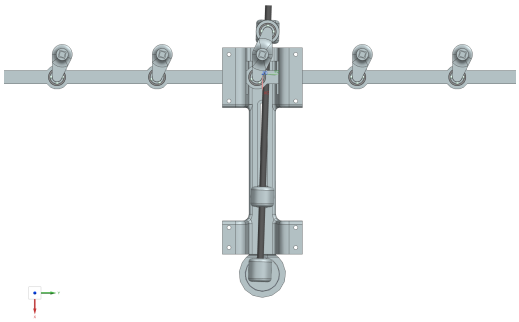

**Figure 3.18:** 30° rotation

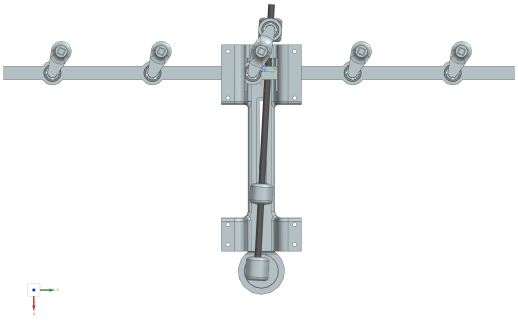

**Figure 3.19:** 60° rotation

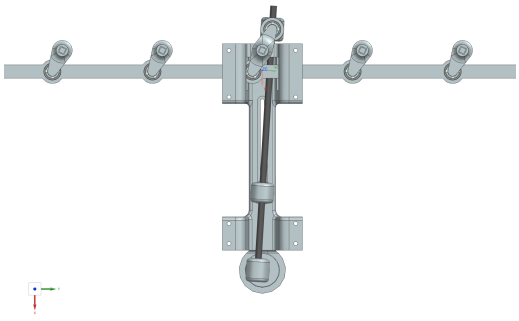

**Figure 3.20:** 90° rotation

The airfoils used in the mechanism are 3D-printed. As shown in Figure 3.21 each airfoil consists of seven segments, one top segment, one bottom segment, and five middle segments. All of these segments are connected via plug-in connections.

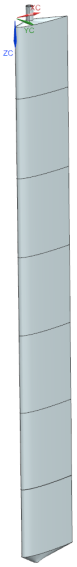

**Figure 3.21:** Complete airfoil with segments

The top segment (Figure 3.22a) has a protruding feature, while the top of the middle segment (Figure 3.22a) has the cavity feature where the two segments are connected together. The same thing can be found on all segments except one middle segment, which has two cavities. Additionally, 3.22b highlights the extended rod integrated to the top segment. This rod is designed to pass through the holes in the upper plate, ensuring mechanical connection and a better distribution of forces.

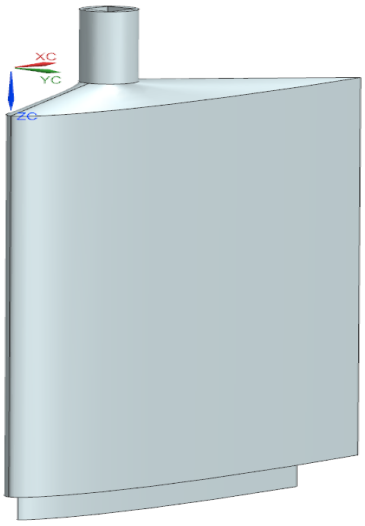

**(a)** Top segment

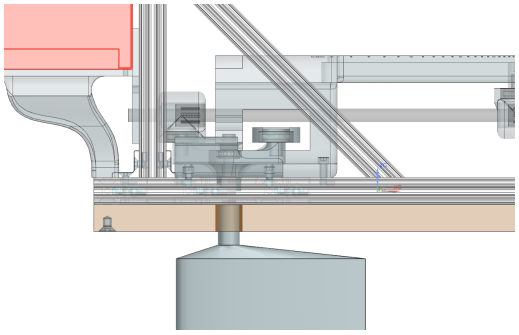

**(b)** Top segment with mounting

**Figure 3.22:** Top segment

The bottom segment (Figure 3.23b) consists of two functional parts. The lower rod extends trough a bearing mounted in the bottom plate for the wing to rotate freely around his axis. On the upper end we have square steel profile, which is being used to increase the rigidity of the wing. Figure 3.23d showcases the deflection of the airfoil without any supporting steel structure. In order to account for tolerances, the wing was designed to house spacers, which enable adjustment in the final stages of assembly. This can be seen in Figure 3.23c.

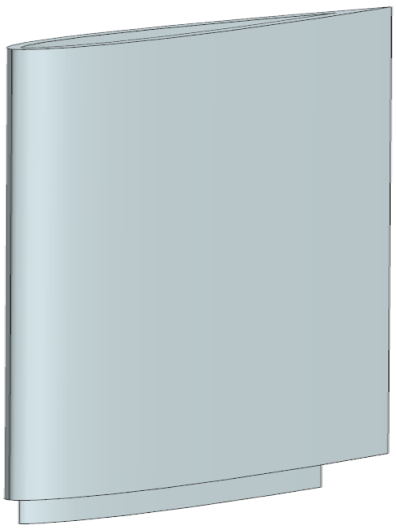

**(a)** Middle segment

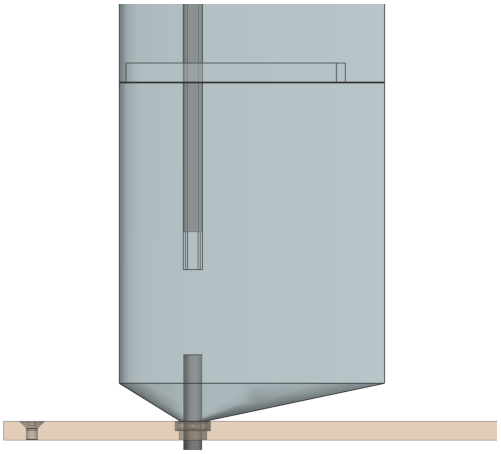

**(b)** Bottom segment

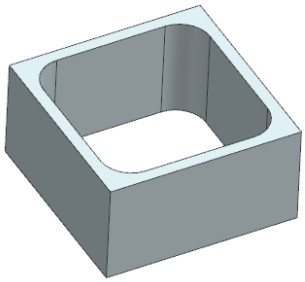

**(c)** Spacer

**(d)** Wing bend without square pipe

**Figure 3.23:** Single segments configuration

## 3.4 Set-up at the Wind tunnel

In this Chapter it will be discussed which steps were taken in order to have a completely mounted mechanism at the wind tunnel. After all parts were printed, the aluminum frame was assembled with all 3D-printed parts from the driving mechanism. At the same time the airfoils were assembled. Once the individual components were assembled, the frame was mounted to the top wooden plate which can be seen in Figure 3.24. This was necessary to avoid a assembly in the final position which would have added complexity because of accessibility.

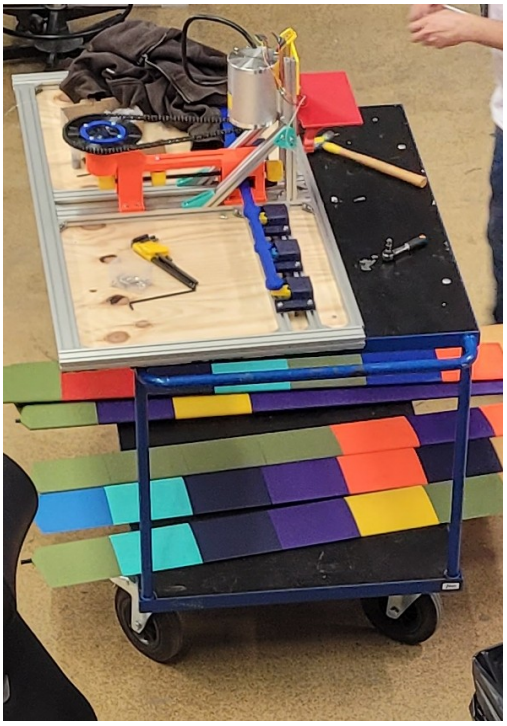

**Figure 3.24:** Aluminum profile with wooden plate

As for the configuration on the top of the wind tunnel it was decided to use the already available four Plexiglas sections (see Fig. 3.25) while replacing the first one with the mechanism. As for the bottom plate, the first black plate has been replaced which can be seen in the same picture.

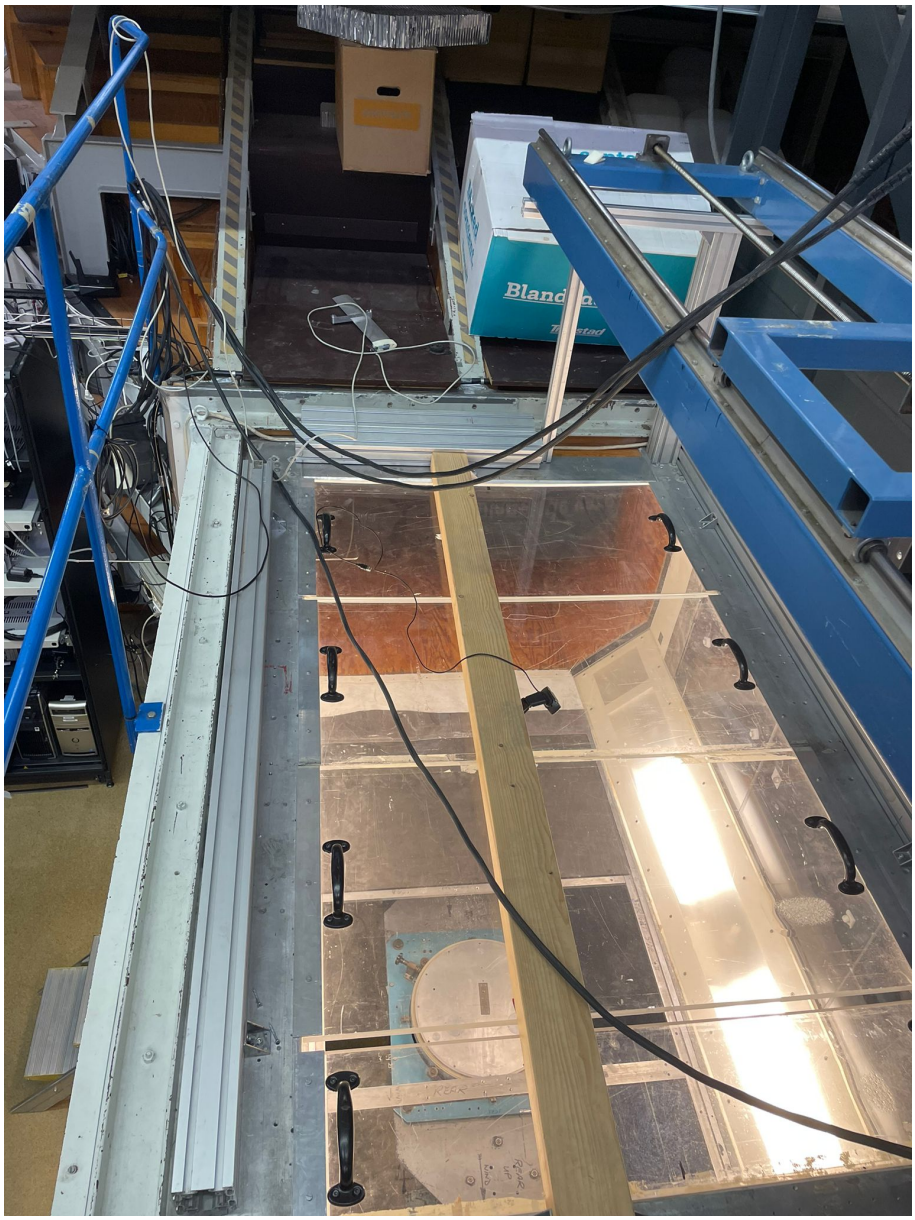

**Figure 3.25:** Top configuration of the wind tunnel

The first step into the wind tunnel was to remove all the Plexiglas panels to have more space to work and to install the top and bottom plates of the mechanism. Once this was done, one person stood in the test section and another one on top of the wind tunnel to install the wings in the right position. The one on top lifted the top plate with the mechanism, while the one in the wind tunnel aligned the wings with the bearings within the bottom plate and with the top plate. With this order of steps, problems with fitting the wings in the connecting parts of the mechanism on top of the wind tunnel were encountered. This was due to the fact that the caps with the connecting axis and the connecting part between the mechanism and wing were already mounted and there was limited freedom to insert the airfoil into the connecting part between the mechanism and wing. For a better comprehension, the caps and the connecting axis are circled in red in Figure 3.26a while the connecting

part between the mechanism and wing is circled in red in Figure 3.26b.

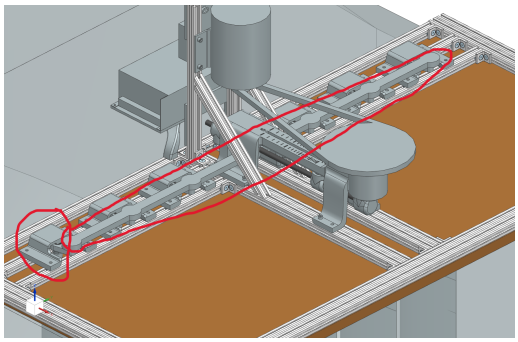

**(a)** Cap and connecting axis

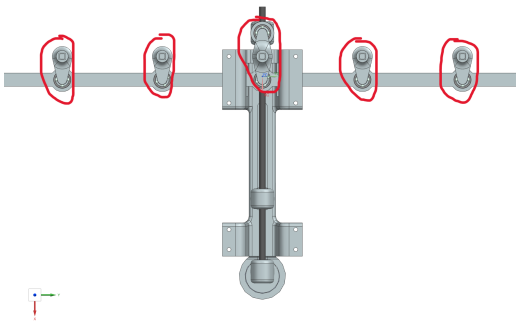

**(b)** Connecting part between the mechanism and wing

**Figure 3.26:** Highlighted parts

For this reason it was decided to unscrew these parts, connect the wing with the connecting part between the mechanism and wing and then screw everything back together.

# 4

# Results

In this Chapter the results from the simulations will be discussed in regard to the turbulence intensity and the turbulent length scales.

## 4.1 CFD-Results

In order to assess the performance of the turbulence generator, two parameter sweeps were simulated. In the first sweep, the maximum angle of attack was fixed to 20° while the frequency was varied from 3Hz to 7Hz in 1Hz steps. In the second sweep, the frequency was fixed to 5Hz the maximum angle of attack was varied from 15° to 25° in 2.5° steps. To visualize the results, the values for the turbulence intensity and turbulent length scale were averaged across test sections. Figure 4.1 shows the presentation grids used for this averaging. Figure 4.2 shows the position of the XY-plane and the XZ-plane relative to the vehicle and the wind tunnel.

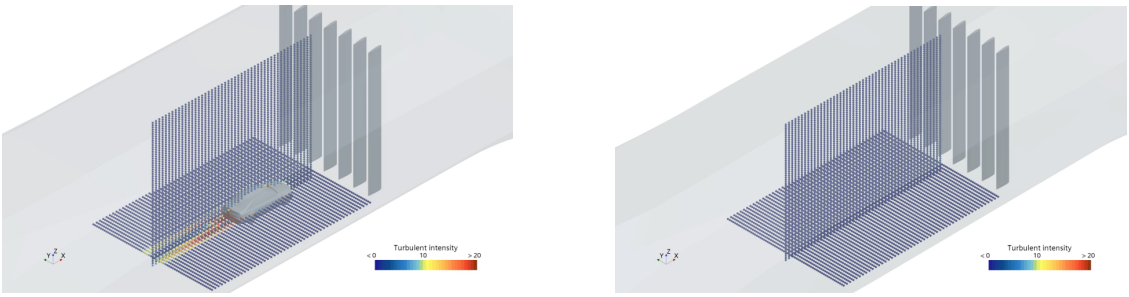


**(a)** Presentation grid with vehicle **(b)** Presentation grid without vehicle

**Figure 4.1:** Presentation grids with and without vehicle

**(a)** Top view **(b)** Side view

**Figure 4.2:** Top and side view

### 4.1.1 Turbulence intensity

Figure 4.3 shows a comparison between the frequency sweep (Figure 4.3a) and the angle sweep (Figure 4.3b). The frequency sweep shows a variation in turbulence intensity of about 0.5% with lower frequencies generating slightly higher intensities. By looking at the angle sweep an increase of about 2% can be seen. This is due to the fact that the separation of the airfoil is beginning much earlier in bigger angle position that in the smaller one.

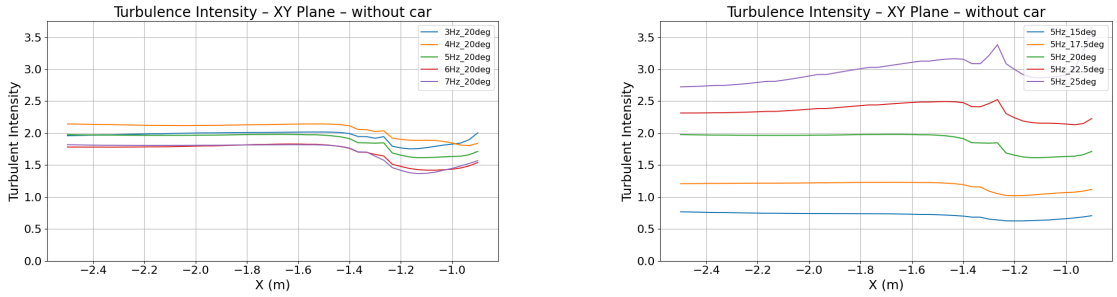


**(a)** Frequency sweep **(b)** Angle sweep

**Figure 4.3:** Turbulence intensity without vehicle (XY-plane in X-direction)

Looking into the comparison of the XY-plane in x-direction with the vehicle inside the domain (Figure4.4) it can be seen that in front of the vehicle, between -0.5m and -1.2m the trend is similar to the case without the vehicle ( see Figure 4.3). However distinct peaks appear in turbulence intensity due to the interaction of the flow with the vehicle's geometry. Figure 4.5 illustrates this effect for the last timestep in the 5Hz 25° configuration. It can be seen that turbulence intensities increases significantly around the wheel housing, which explains the first two peaks in both plots in Figure 4.4. However taking a closer look at the diagrams it can be seen that they have the same behavior of the beginning of the plot that the higher turbulence intensities that are in front of the vehicle also have the higher peaks. This can only be clearly seen on the angle sweep Figure 4.4b but on the frequency sweep Figure 4.4a there are not many changes between the frequencies as also seen before. Beyond the vehicle around -1.7m the wake occurs and rises the turbulence intensity

to a maximum of about 16.5%. here a switch on the trend of the two sweeps can be seen. For the frequency sweep, turbulence intensity decreases with increasing frequency, dropping from 16.5% down to 13%, while the angle sweep shows only minor variations of approximately 1% in this region. After the last peak on both plots the turbulence intensities tends to converge at the end of the test section but maintain the same behavior as the beginning of the test section. However, even if they maintain the same behavior of the inlet, in overall they increase the turbulence intensity of about 1-2%.

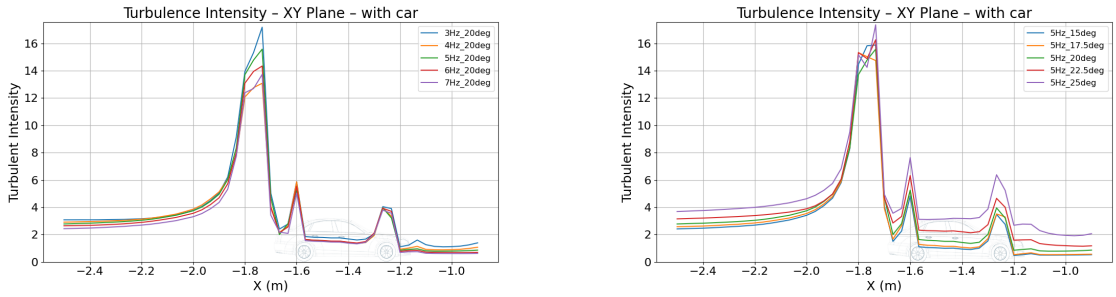


**(a)** Frequency sweep **(b)** Angle sweep

**Figure 4.4:** Turbulence intensity with vehicle (XY-plane in X-direction)

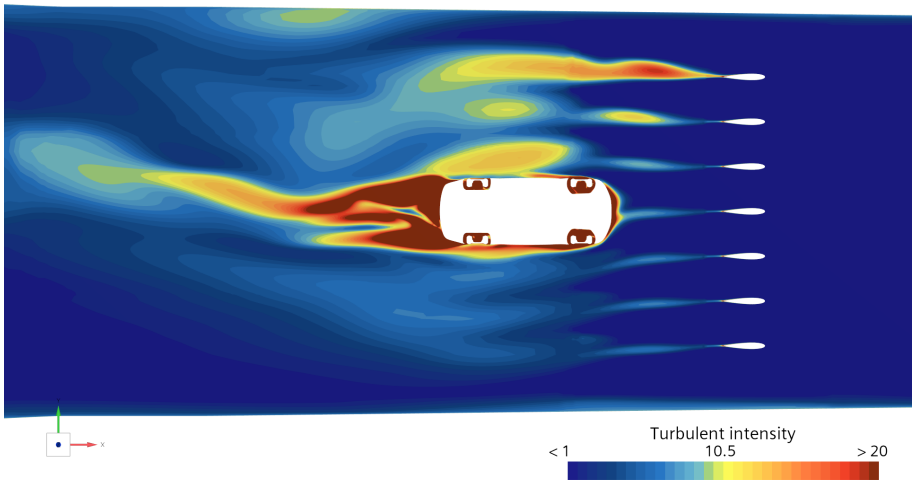


**Figure 4.5:** XY-plane Section of turbulence intensity in X-direction at 5Hz_25deg for better understanding of the peaks

When examining the lateral distribution (Y-direction), a similar pattern emerges. However, when looking at Figure 4.6b it can be seen that at the outermost sides of the wind tunnel there are some peaks and then in the middle section it drops again down. This is due to the fact that the outer wings do not have adjacent wings at the tunnel's outer edges, causing an earlier flow separation there and therefore increasing the turbulence intensity.

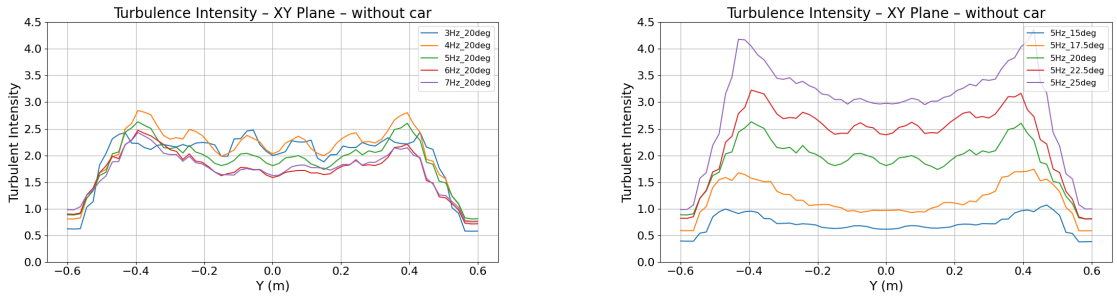


**(a)** Frequency sweep **(b)** Angle sweep

**Figure 4.6:** Turbulence intensity without vehicle (XY-plane in Y-direction)

With the vehicle inside the domain (Figure 4.7) it can be seen how the wake increases the turbulence intensity and going up to 25% in the middle of the test section. Moving further away from the vehicle the turbulence intensity decreases. For the frequency sweep ( Figure 4.7a) low values around 2-2.5% were achieved, while at the angle sweep ( Figure 4.7b) it can be seen how the turbulence intensity can vary from 1-4% based on which angle of attack is chosen. Lower angles lead to low turbulence intensities while larger angles give higher turbulence intensities leading to the same behavior seen before.

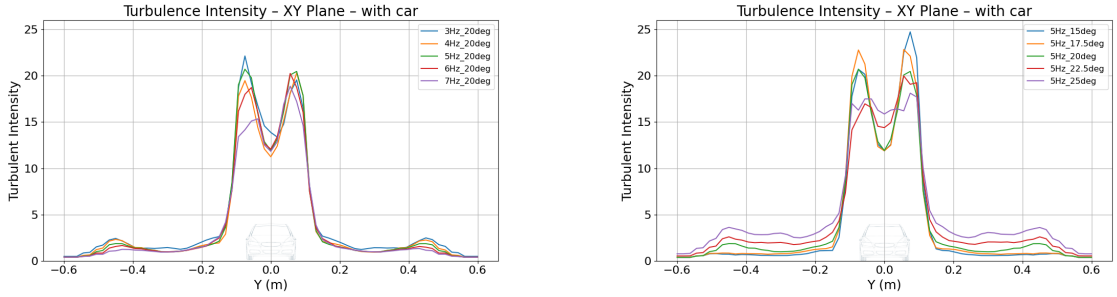


**(a)** Frequency sweep **(b)** Angle sweep

**Figure 4.7:** Turbulence intensity with vehicle (XY-plane in Y-direction)

Comparing the sweeps in the XY-plane with and without the vehicle (see Figure4.8) it can be observed that they behave similarly in front of the vehicle along the X-direction. However, behind the vehicle, after the peak of the wake, the turbulence intensity increases by approximately 1% when the vehicle is placed inside the domain. In the Y-direction, the general trend remains consistent with and without the vehicle. Between $\pm 0.2$ and $\pm 0.6$, the peaks corresponding to the outer wings are visible around $\pm 0.4$. Moving further to the center, the turbulence intensity decreases, but then increases again at the very center in the plots with the vehicle due to the wake generated behind it.

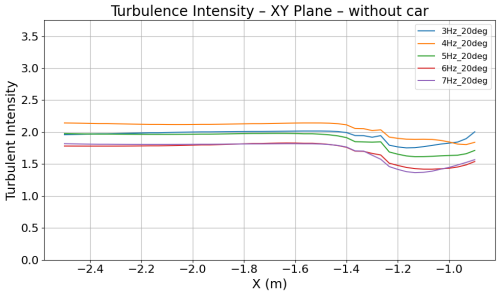


**(a)** Frequency sweep (XY-plane in X-direction) without vehicle

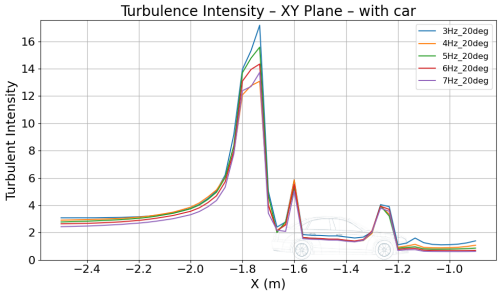


**(b)** Frequency sweep (XY-plane in X-direction) with vehicle

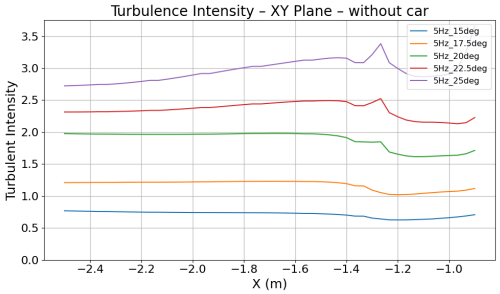


**(c)** Angle sweep (XY-plane in X-direction) without vehicle

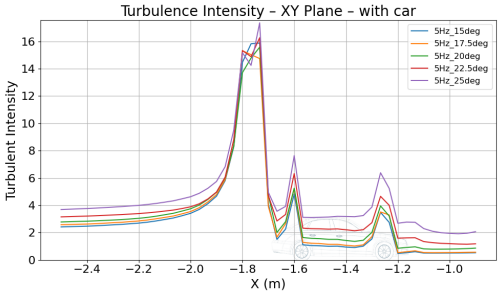


**(d)** Angle sweep (XY-plane in X-direction) with vehicle

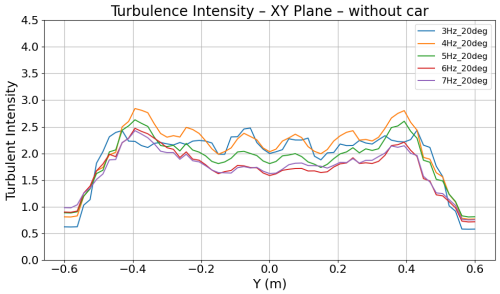


**(e)** Frequency sweep (XY-plane in Y-direction) without vehicle

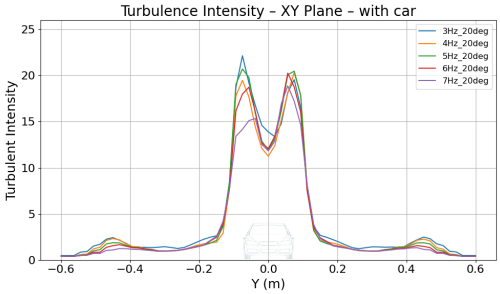


**(f)** Frequency sweep (XY-plane in Y-direction) with vehicle

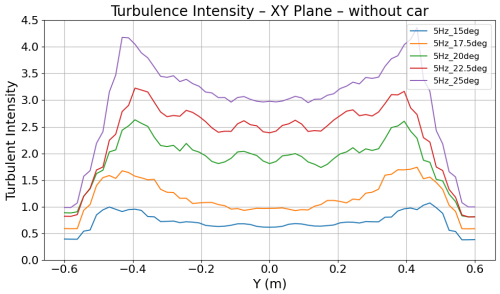


**(g)** Angle sweep (XY-plane in Y-direction) without vehicle

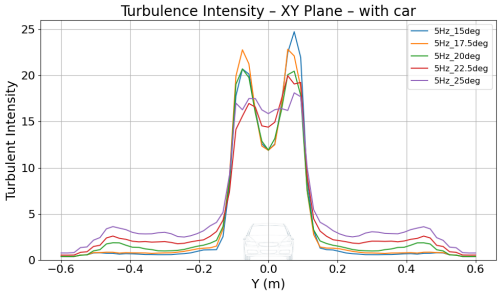


**(h)** Angle sweep (XY-plane in Y-direction) with vehicle

**Figure 4.8:** Turbulence intensity comparisons: frequency and angle sweeps with and without vehicle (XY-plane, X and Y-directions).

The following section discusses the results obtained in the XZ-plane, both with and without the vehicle. Looking at Figure 4.9 it can be observed that the angle sweep ( Figure4.9b) has an higher turbulence intensity compared to the frequency sweep ( Figure4.9a). At the beginning of the test section the configuration with 25° of maximum angle of attack reaches turbulence intensities of about 29%, while the second largest one reaches only $\approx 15\%$. As for the other configurations, the smaller the angle the lower the turbulence intensity. Additionally, it can be noted that towards the end of the test section, the turbulence intensity tends to converge. For the angle sweep, although the turbulence intensity is predominantly influenced by the angle of attack, the difference between the angles become less pronounced further downstream. In the frequency sweep, the turbulence intensities starts at similar values for all frequencies, with the lower frequencies reaching about 10% while the higher frequencies are at $\approx 6 - 7\%$. Interestingly, at the end of the test section, all frequencies converge to the same point.

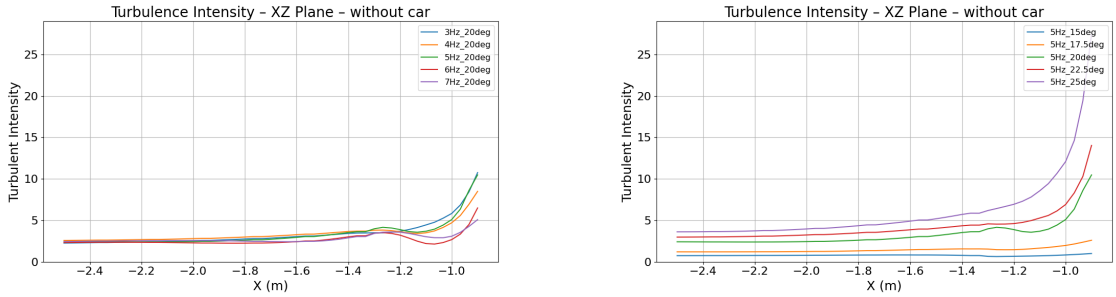


**(a)** Frequency sweep **(b)** Angle sweep

**Figure 4.9:** Turbulence intensity without vehicle (XZ-plane in X-direction)

In Figure 4.10, the same plane and direction as in the previous figure are presented, but this time the vehicle is included in the test section. When comparing both plots, it is evident that both display two peaks at the same position in x. One at $\approx -1.6m$ and one at $\approx -1.8m$. The peak at $-1.6m$ corresponds to a small increase in turbulence intensity, caused by a recirculation region of the rear windshield, which enhances the turbulence. The second peak, at about $-1.7m$ and $-1.8m$ is due to the wake region behind the vehicle. The turbulence intensity here is lower compared to the peak observed in Figure 4.4 because this plot represents the turbulence intensity averaged over the entire height of the test section and not only behind the vehicle.

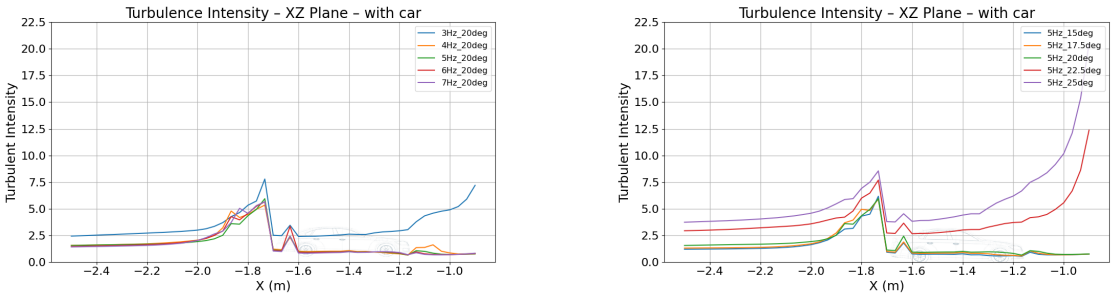


**(a)** Frequency sweep **(b)** Angle sweep

**Figure 4.10:** Turbulence intensity with vehicle (XZ-plane in X-direction)

The analysis then shifts to the z-direction, as shown in Figures 4.11 and 4.12. For these plots, the axes have been reoriented for better understanding. The y-axis now represents the height of the test section, while the x-axis shows the turbulent intensity. In Figure 4.11b, where no vehicle is present, it can be observed that the turbulence intensity is lower near the top and bottom walls due to the viscous sublayer, while it increases towards the center of the wind tunnel, reaching levels of up to 8%. This behavior becomes more pronounced as the angle of attack increases, leading to higher overall turbulence intensities. In Figure 4.12, it is apparent that between heights of $-0.6m$ to $-0.5m$, the turbulence intensity increases for both the angle and the frequency sweeps. This is attributed to the presence of the vehicle at this height within the test section, which results in elevated turbulence intensities caused by the wake behind the vehicle.

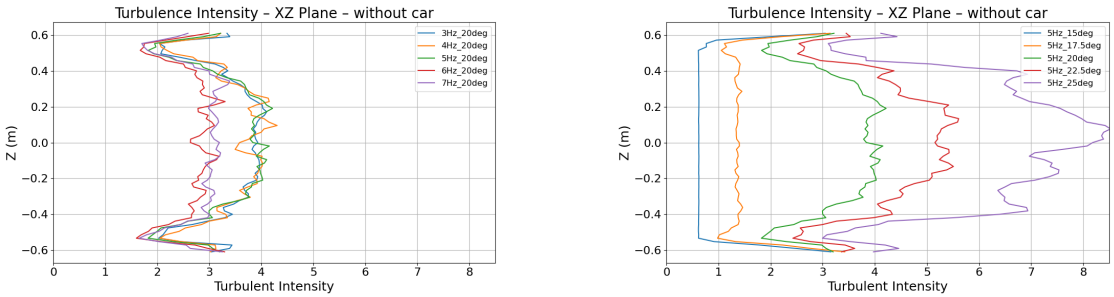


**(a)** Frequency sweep **(b)** Angle sweep

**Figure 4.11:** Turbulence intensity without car (XZ-plane in Z-direction)

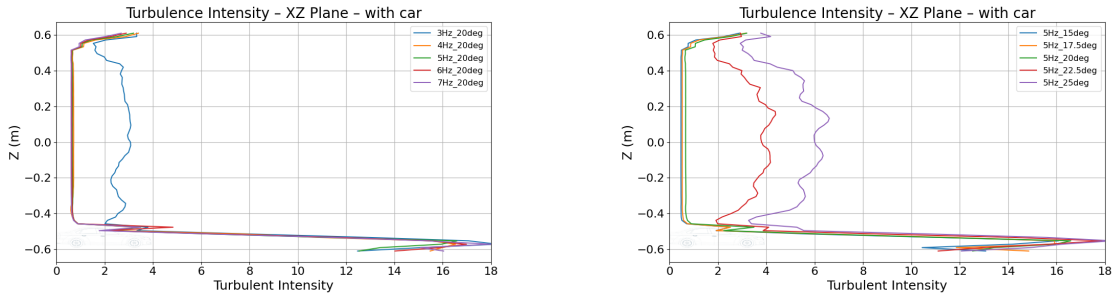


**(a)** Frequency sweep **(b)** Angle sweep

**Figure 4.12:** Turbulence intensity with vehicle (XZ-plane in Z-direction)

Finally, comparing the corresponding plots for the same plane and direction with the identical sweep type, with and without the vehicle (Figures 4.13 to 4.16), it can be seen that their behavior remains almost the same, with the exception of the wake regions influenced by the presence of the vehicle.

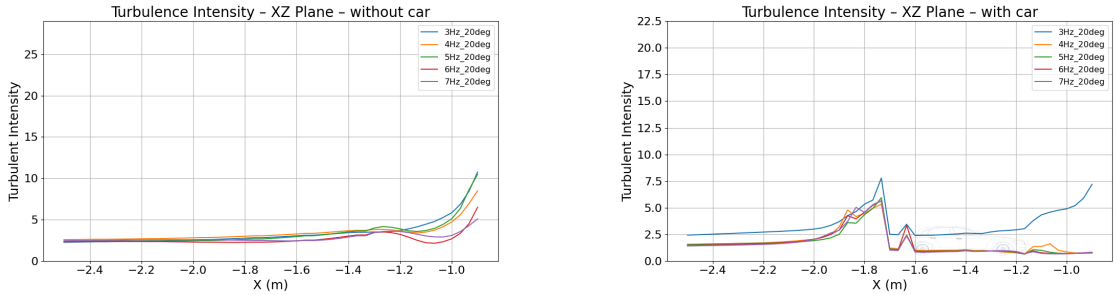


**(a)** Without vehicle **(b)** With vehicle

**Figure 4.13:** Turbulence intensity comparison frequency sweep (XZ-plane in X-direction)

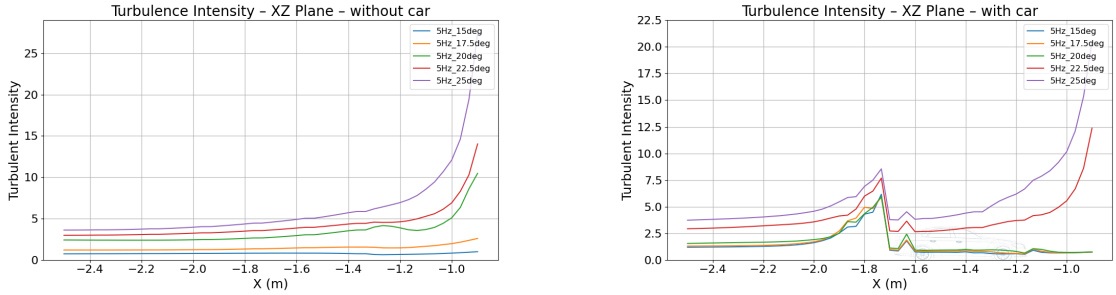


**(a)** Without vehicle **(b)** With vehicle

**Figure 4.14:** Turbulence intensity comparison angle sweep (XZ-plane in X-direction)

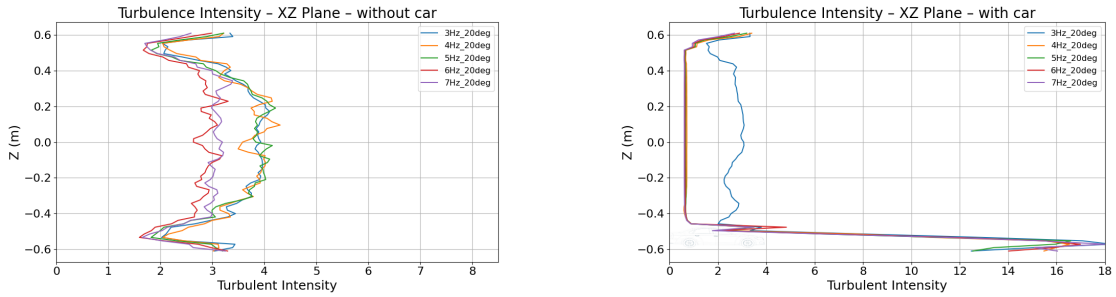


**(a)** Without vehicle **(b)** With vehicle

**Figure 4.15:** Turbulence intensity comparison frequency sweep (XZ-plane in Z-direction)

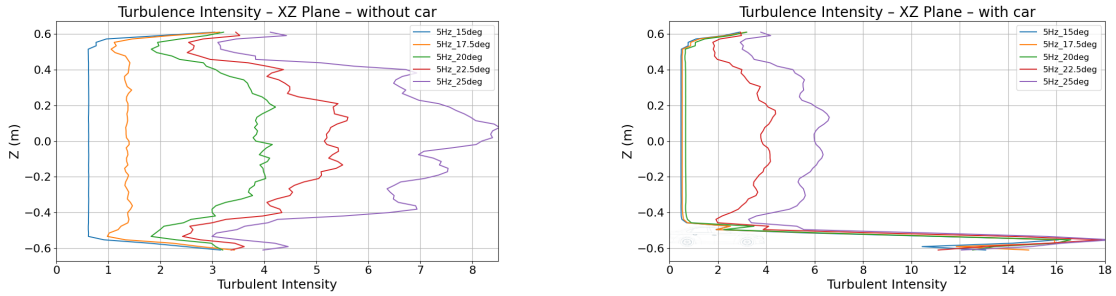


**(a)** Without vehicle **(b)** With vehicle

**Figure 4.16:** Turbulence intensity comparison angle sweep (XZ-plane in Z-direction)

### 4.1.2 Turbulent length scale

Starting with Figure 4.17, the behavior of the turbulent length scale in the XY-plane along the X-direction without the vehicle can be observed. The frequency sweep (Figure4.18a) shows that the turbulent length scale does not vary significantly with increasing frequency. Instead, it changes with distance downstream. Here, the turbulent length scale starts at approximately $1cm$ and increases to around $4.3cm$ after $1.5m$. In contrast, in the angle sweep (Figure4.17b), all angles of attack begin with a turbulent length scale between $\approx 1.2cm$ to $\approx 1.5cm$, but the increase of the eddies differs greatly. The smallest angle of attack (15°) results in a final turbulent length scale of $\approx 2.3cm$ having an increase of about $1cm$ over the entire distance. The largest angle of attack (25°) results in a turbulent length scale of approximately $5cm$, representing an increase of $3.5cm$ over $1.5m$.

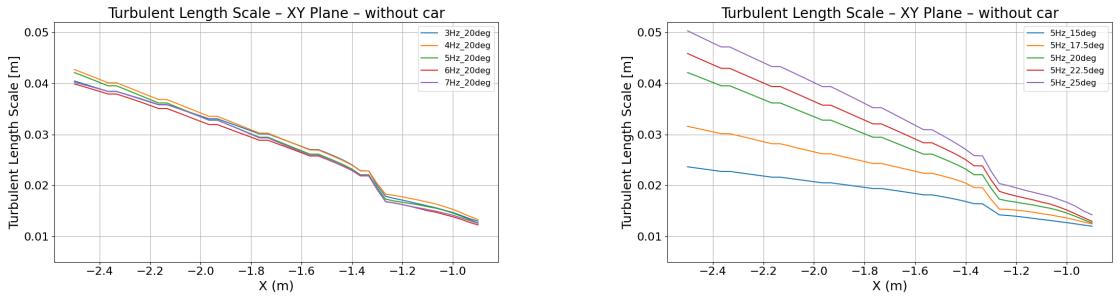


**(a)** Frequency sweep **(b)** Angle sweep

**Figure 4.17:** Turbulent length scale without vehicle (XY-plane in X-direction)

When examining the sweeps with the vehicle inside the domain ( Figure 4.18) it can be observed that there are spikes near the front windshield, rear windshield and within the wake region behind the vehicle. Overall, the behavior remains consistent with previous observations. The angle sweep has a larger impact on the turbulent length scale than the frequency sweep.

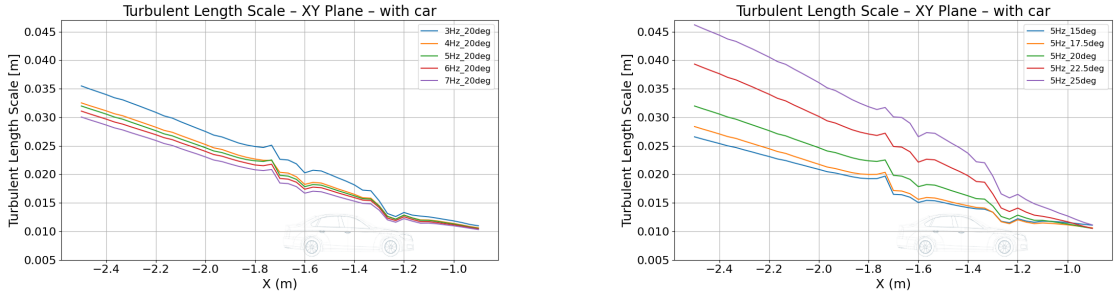


**(a)** Frequency sweep **(b)** Angle sweep

**Figure 4.18:** Turbulent length scale with car (XY-plane in X-direction)

Considering now the plots along the width of the test section ( Figures 4.19 and Figure 4.20), the frequency sweep without the vehicle ( Figure 4.19a) shows relatively consistent turbulent length scale across the section. However, the angle sweep ( Figure 4.19b) again demonstrates a great impact on the eddy size. The smallest angle of attack results in eddies of about $1.5cm$, while at 25° of angle of attack the eddies reach sizes of approximately $3.5cm$. With the vehicle included ( Figure4.20), both the frequency and angle sweeps show an increase in turbulent length scales to $\approx 3.25cm$ in the center. Moving towards the side walls, the eddies in the angle sweep ( Figure4.20b) have a larger size compared to those in the frequency sweep ( Figure 4.20a).

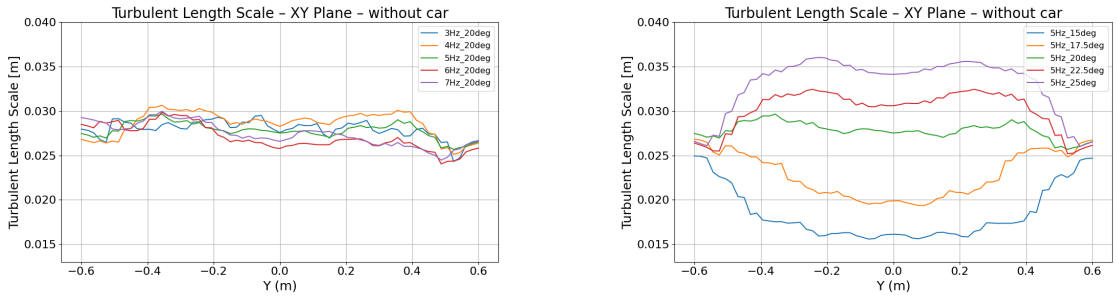


**(a)** Frequency sweep **(b)** Angle sweep

**Figure 4.19:** Turbulent length scale without vehicle (XY-plane in Y-direction)

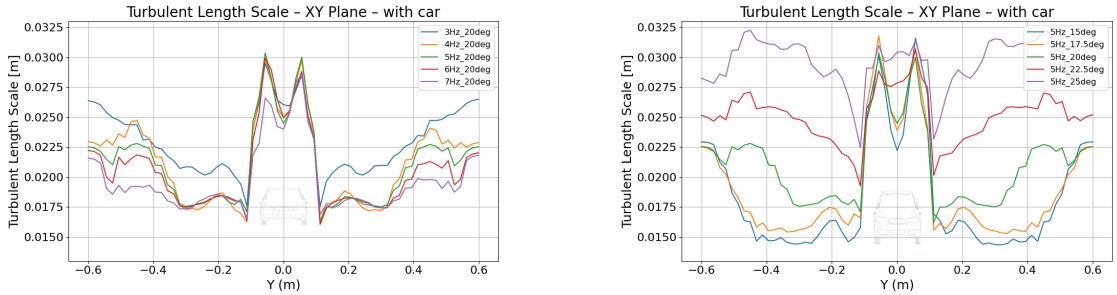


**(a)** Frequency sweep **(b)** Angle sweep

**Figure 4.20:** Turbulent length scale with vehicle (XY-plane in Y-direction)

By comparing the plots of the same sweeps with and without the vehicle ( see Figures 4.21 and 4.22), it is evident that in the XY-Plane along the X-direction, the presence of the vehicle does not significantly alter the turbulent length scale, except for small peaks at the windshields and in the wake region. However, along the Y-direction, differences between the frequency sweeps with and without the vehicle ( Figures 4.22a and 4.22b ) are notable. Excluding the wake region behind the vehicle, which produces the largest eddies, it can be seen that towards the side walls, the turbulent length scales remain mostly linear in the absence of the vehicle, ranging from 2.6$cm$ to 3$cm$ across all frequencies. In the presence of the vehicle, the range is slightly lower, from approximately 1.75 cm to 2.7 cm. For the angle sweep (Figures 4.22c and 4.22d), the turbulent length scale shows little variation between both with and without the vehicle, except in the wake region where a significant increase is observed.

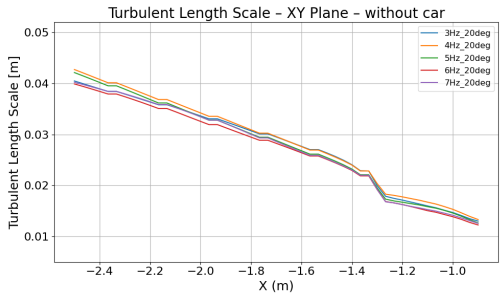


**(a)** Frequency sweep without vehicle

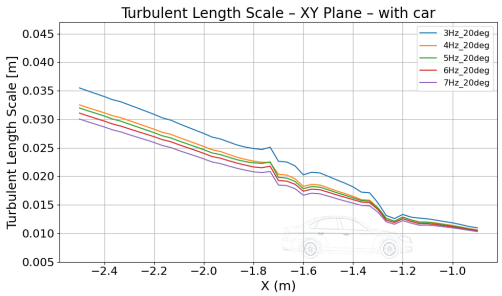


**(b)** Frequency sweep with vehicle

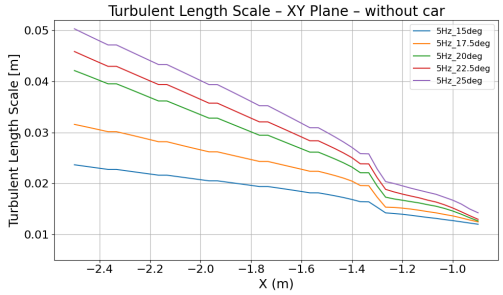


**(c)** Angle sweep without vehicle

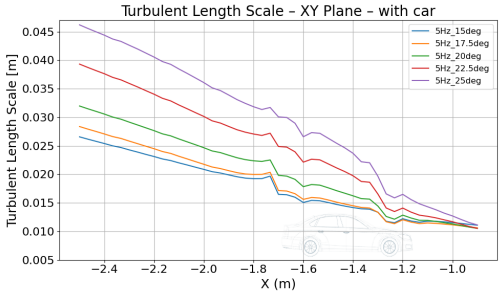


**(d)** Angle sweep with vehicle

**Figure 4.21:** Turbulent length scales: frequency and angle sweeps with and without vehicle (XY-plane, X-direction).

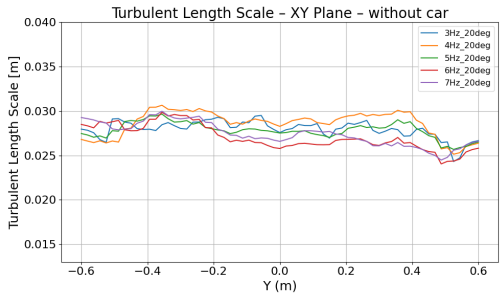


**(a)** Frequency sweep without vehicle

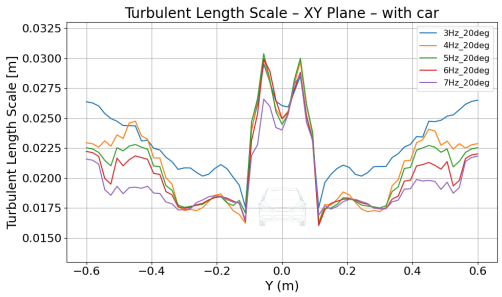


**(b)** Frequency sweep with vehicle

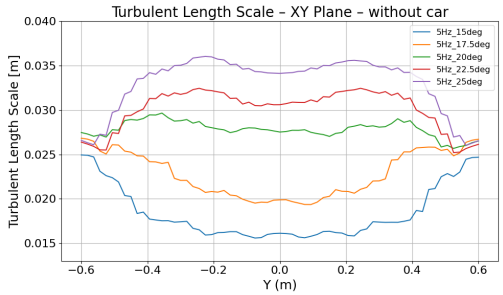


**(c)** Angle sweep without vehicle

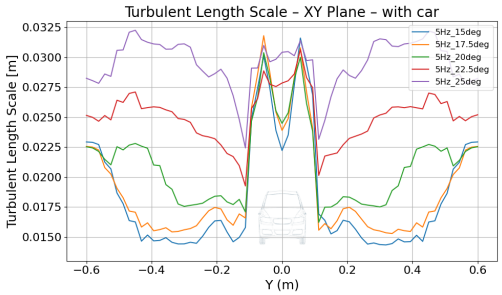


**(d)** Angle sweep with vehicle

**Figure 4.22:** Turbulent length scales: frequency and angle sweeps with and without vehicle (XY-plane, Y-direction).

Now, the sweeps thorough the XZ-Plane with and without the vehicle are discussed. Along the X-direction without the vehicle ( Figure 4.23), can be observed that variations in frequencies ( Figure4.23a) do not have a significant effect on the turbulent length scale. The eddy size begins at approximately 1.5$cm$ and grows up until 5$cm$. In contrast, the angle sweep ( Figure 4.23b) shows a considerable spread in eddy sizes depending on the angle of attack. At 15°, the eddies start slightly below 1$cm$ and end around 2$cm$, while the largest angle at 25°, the eddies start around 2.2$cm$ and grow up to approximately 6.5$cm$.

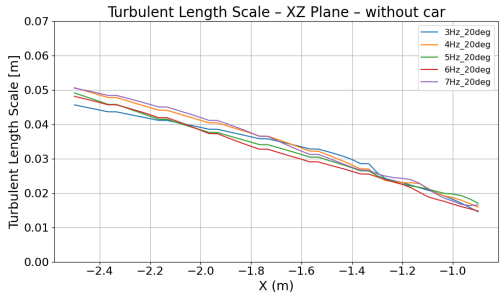


**(a)** Frequency sweep

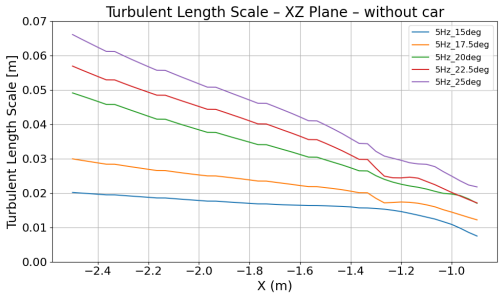


**(b)** Angle sweep

**Figure 4.23:** Turbulent length scale without car (XZ-plane in X-direction)

The turbulent length scale in the XZ-Plane along the X-direction with vehicle ( Figure4.24), shows a slightly different behavior from previous observations. In the frequency sweep ( Figure4.24a), all frequencies produce similar turbulent length scales, except for the $3Hz$ simulation, which starts around $0.3cm$ higher and ends up with a turbulent length scale approximately $1.5cm$ larger. The angle sweep ( Figure4.24b) also displays an unusual behavior. Here, the angles from 15° to 20° behave quite similar, starting at $0.6cm$ and ending at around $0.2cm - 0.25cm$, while the 22.5° and the 25° generate larger eddies. The 22.5° angle begins with eddies of $1.25cm$ and increases up to $5cm$, while the 25° angle shows an initial offset of approximately $0.5cm$ and ends with an offset of around $1cm$ compared to the 22.5° case.

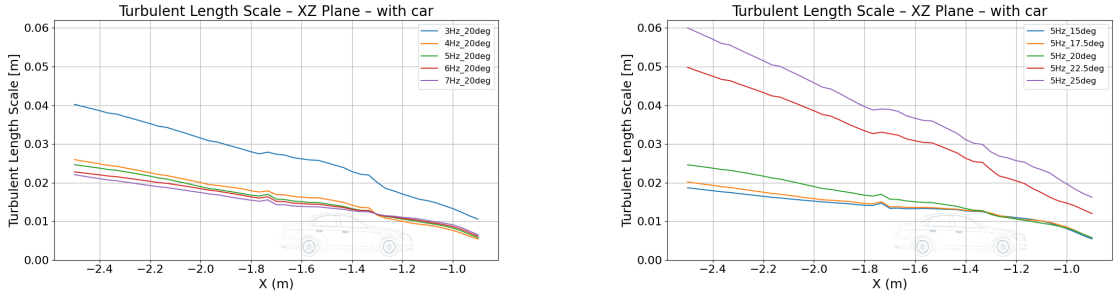


**(a)** Frequency sweep **(b)** Angle sweep

**Figure 4.24:** Turbulent length scale with car (XZ-plane in X-direction)

Figure 4.29 shows how the turbulent length scale varies with height throughout the test section. This behavior is similar to that of the turbulence intensity distribution shown in Figure 4.11. Near the walls, where the viscous sub layer is present, the turbulent length scale is smaller, whereas towards the center of the section the eddies increase. The general trend between the frequency and angle sweeps remains consistent, with the angle sweep producing eddies ranging from approximately $1.5cm$ to $5cm$ depending on the angle of attack, while all frequencies in the frequency sweep produce similar eddies sizes of around $3.5cm$.

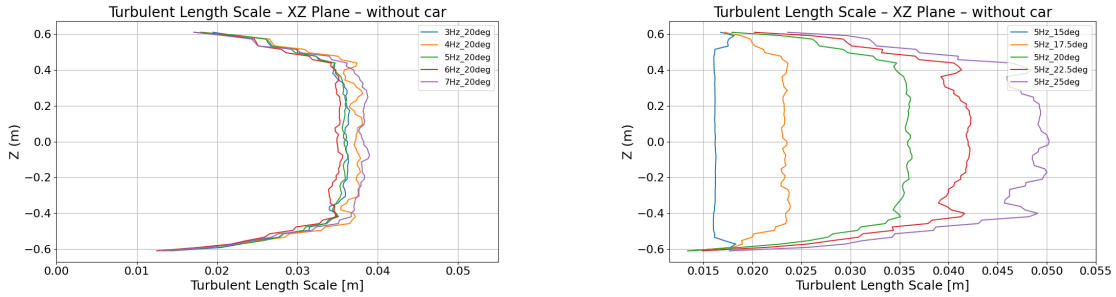


**(a)** Frequency sweep **(b)** Angle sweep

**Figure 4.25:** Turbulent length scale without car (XZ-plane in Z-direction)

Figure 4.26 shows the same plot as Figure 4.29, but with the vehicle included in

the wind tunnel. It can clearly be seen that the vehicle influences the flow up to $\approx -0.45m$, corresponding to the wake region behind the vehicle. Afterwards, the turbulent length scale exhibits a behavior similar to that in Figure 4.29. In the frequency sweep ( Figure 4.26a), the 3Hz run produces increased turbulent length scales, while the angle sweep only the two largest angles of attack show a noticeable increase, with the other angles remaining relatively similar to each other.

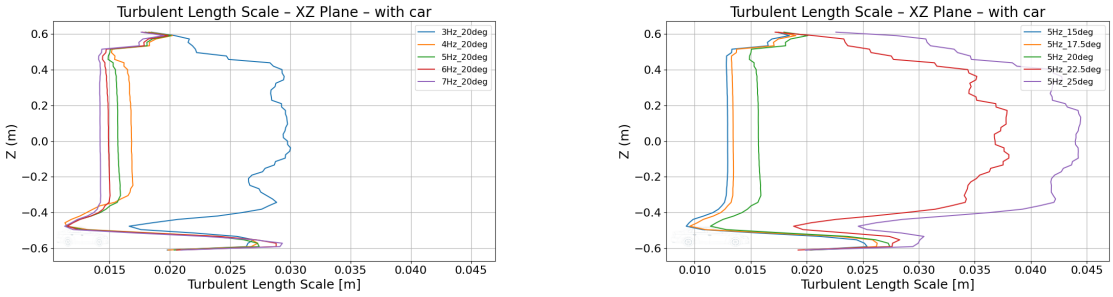


**(a)** Frequency sweep **(b)** Angle sweep

**Figure 4.26:** Turbulent length scale with car (XZ-plane in Z-direction)

Finally, by comparing the same sweeps with and without the vehicle for the XZ-Plane in both the X- and Z-directions ( see Figure4.27), it is evident how the results behave nearly identical in regions unaffected by the vehicle, with the primary differences occurring within the wake region. Additionally, it can be observed that for the frequency sweep, the 3 Hz simulation results in a higher turbulent length scale compared to the other frequencies. For the angle sweep, the 22.5° and 25° cases produce larger eddies compared to the lower angles, which remain similar. In contrast, in the plots without the vehicle, clearer differences are visible between all angles.

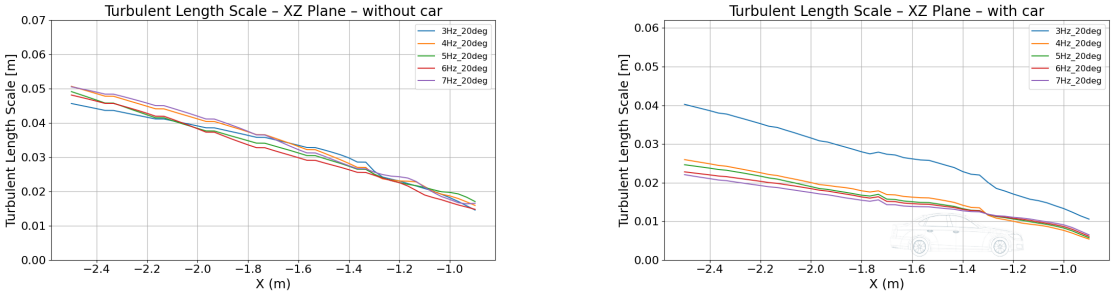


**(a)** Frequency sweep X-direction without car **(b)** Frequency sweep X-direction with car

**Figure 4.27:** Turbulent length scales: frequency and angle sweeps with and without car (XZ-plane, X, Z-direction).

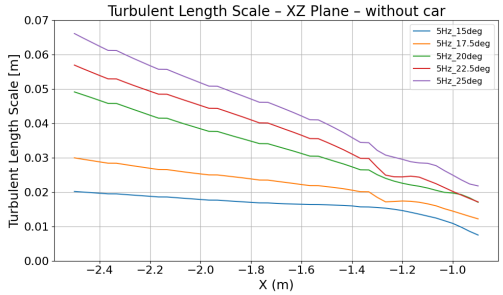


**(c)** Angle sweep X-direction without vehicle

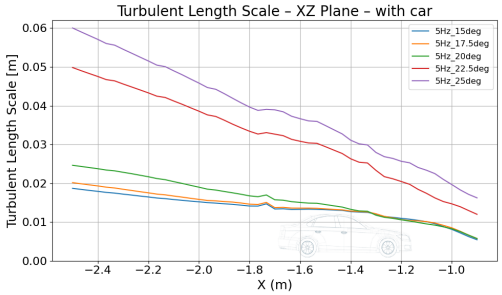


**(d)** Angle sweep X-direction with vehicle

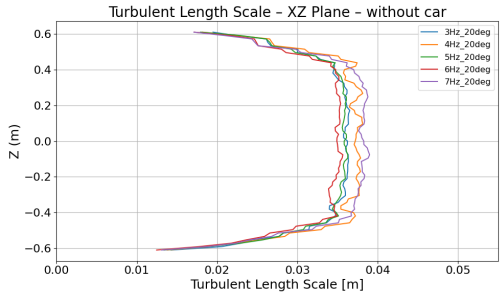


**(e)** Frequency sweep Z-direction without vehicle

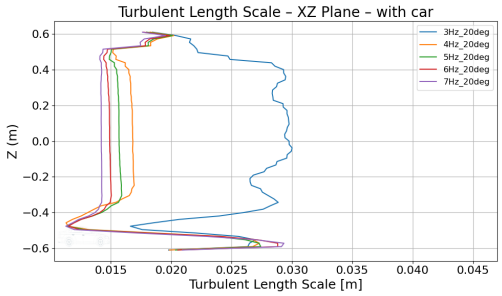


**(f)** Frequency sweep Z-direction with vehicle

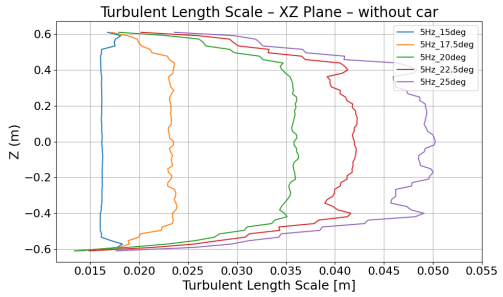


**(g)** Angle sweep Z-direction without vehicle

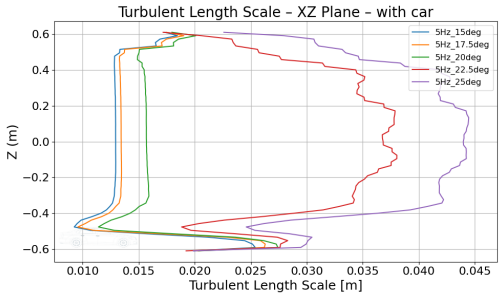


**(h)** Angle sweep Z-direction with vehicle

**Figure 4.27:** Turbulent length scales: frequency and angle sweeps with and without vehicle (XZ-plane, X, Z-direction).

### 4.1.3 Aerodynamic coefficients

When analyzing the aerodynamic drag coefficient ($c_d$), it can be seen that with increasing frequency, as well as with increasing angle of attack, the drag coefficient increases. This is due to the increase of turbulence intensity and turbulence length scale. However, the lowest angle of attack had a significant higher value for $c_d$ compared to 17.5° angle of attack. This behavior couldn't be explained and should be tested in the wind tunnel

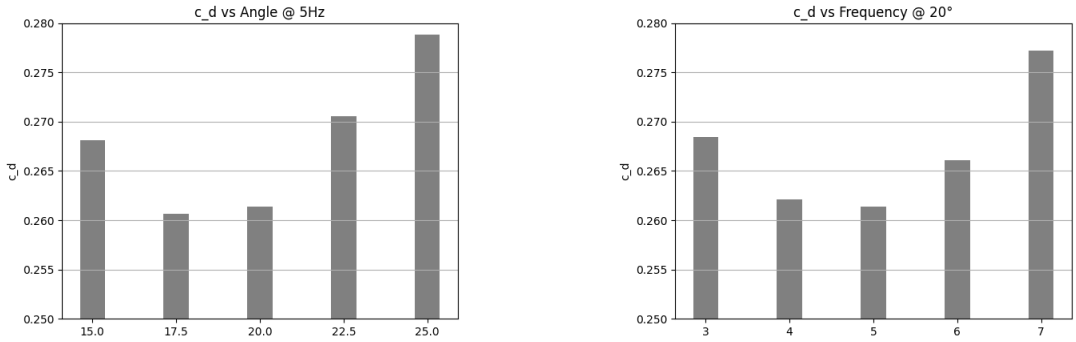


**(a)** Angle sweep **(b)** Frequency sweep

**Figure 4.28:** Aerodynamic drag coefficient comparison

For the aerodynamic lift coefficient the angle sweep and the frequency sweep show two different trends. For the angle sweep, $c_l$ increases up until 22.5°. For the frequency sweep, no clear trend is shown, which indicates that the frequency has no significant influence on $c_l$

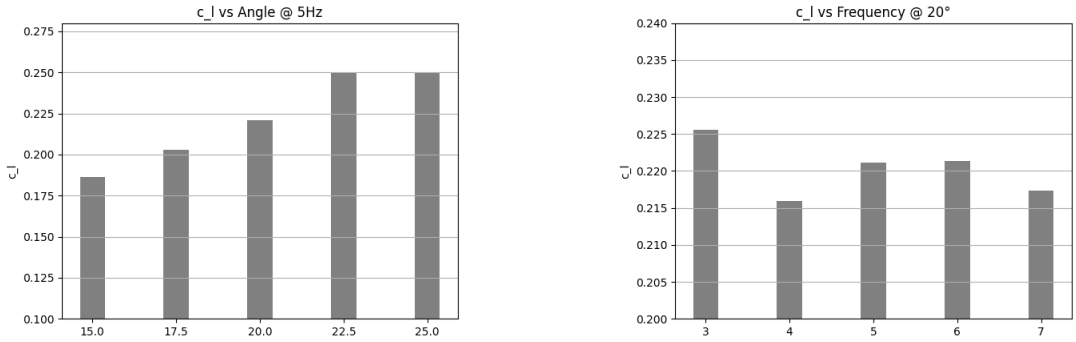


**(a)** Angle sweep **(b)** Frequency sweep

**Figure 4.29:** Aerodynamic lift coefficient comparison

# 5
# Conclusion

The objective of this thesis was to develop and validate an active turbulence generator capable of reproducing real-world turbulence characteristics within a model-scale wind tunnel environment. After a successful virtual design and simulation of the system, the turbulence generator was successfully installed in the wind tunnel. However, due to unforeseen external circumstances, experimental testing in the wind tunnel could not be carried out as planned.

## 5.1 Future Improvements

The system can be improved by a more reliable electric drivetrain, which caused connectivity issues when installed in the final position. Furthermore, the chain connecting the mechanism and the motor needs some additional guidance to reduce the chance of derailing. Another area for improvement is the installation of the turbulence generator. In the current setup, all seven wings need to be connected simultaneously. This turned out to be extremely challenging and could be improved by adding chamfers to the connection points between the steel profile and the mechanism on top of the tunnel. As for the moving wings, future improvements can also be made. One is to reduce the angle of attack of the outer wings so that the turbulence intensity does not have any peaks at the outermost positions and an additional improvement that can be done is to change the mechanism of the connecting parts to the wings so that the wings can move out of phase and increase more the generated turbulence inside the wind tunnel.

# Bibliography


[1] CFD Online. *Turbulence Intensity*. `https://www.cfd-online.com/Wiki/Turbulence_intensity`. Accessed: 2025-02-05. n.d.

[2] Bradley Duncan et al. "Vehicle aerodynamics impact of on-road turbulence". In: *Proceedings of the Institution of Mechanical Engineers, Part D: Journal of Automobile Engineering* 231.9 (2017), pp. 1148–1159.

[3] Joel H Ferziger, Milovan Perić, and Robert L Street. *Numerische strömungsmechanik*. Vol. 1. Springer, 2008.

[4] Karim Ghaib. *Einführung in die numerische Strömungsmechanik*. Springer, 2019.

[5] Joel Guerrero. *Turbulence and CFD models:Theory and applications (lecture 2)*. http://www.dicat.unige.it/guerrero/turbulence2021/slides/lecture2/2tur$_p reliminaries.pdf$ 2021.

[6] Joel Guerrero. *Turbulence and CFD models:Theory and applications (lecture 3)*. http://www.dicat.unige.it/guerrero/turbulence2021/slides/lecture3/3turbulence$_S cales_l aw_o$ 2021.

[7] Joel Guerrero. *Turbulence and CFD models:Theory and applications (lecture 6)*. http://www.dicat.unige.it/guerrero/turbulence2021/slides/lecture6/6closure$_m odels_R ANS_p$ 2021.

[8] idealsimulations. *Turbulence models in CFD*. Visited 30.05.2025. URL: `https://www.idealsimulations.com/resources/turbulence-models-in-cfd/`.

[9] Tamás Kalmár-Nagy and Bendegúz Dezső Bak. "An intriguing analogy of Kolmogorov's scaling law in a hierarchical mass–spring–damper model". In: *Nonlinear Dynamics* 95 (2019), pp. 3193–3203.

[10] Wolfgang Kümmel. "Technische Strömungsmechanik, Theorie und Praxis, 2". In: *Auflage, Vieweg+ Teubner* (2007).

[11] Stefan Lecheler. *Numerische Strömungsberechnung*. Springer, 2023.

[12] M Darwish F Moukalled L Mangani, M Darwish, et al. *The Finite Volume Method in Computational Fluid Dynamics*. 2016.

[13] NASA. *Closed Return Wind Tunnel*. Visited 28.05.2025. URL: `https://www.grc.nasa.gov/www/k-12/airplane/tuncret.html`.

[14] NASA. *Open Return Wind Tunnel*. Visited 28.05.2025. URL: `https://www.grc.nasa.gov/www/k-12/airplane/tunoret.html`.

[15] Prof. Håkan Nilsson. "Computational Fluid Dynamics:The Finite Volume Method (CFD)". 2025.

[16] Peng Qin, Alessio Ricci, and Bert Blocken. "CFD simulation of aerodynamic forces on the DrivAer car model: Impact of computational parameters". In: *Journal of Wind Engineering and Industrial Aerodynamics* 248 (2024), p. 105711.

[17] Bastian E Rapp. *Microfluidics: modeling, mechanics and mathematics*. William Andrew, 2016.
[18] Sathiyan et al. "Aerodynamic Investigations of a Simplified Passenger Vehicle".
[19] Thomas Schütz. *Hucho-Aerodynamik des Automobils: Strömungsmechanik, Wärmetechnik, Fahrdynamik, Komfort*. Springer-Verlag, 2023.
[20] Rüdiger Schwarze. *CFD-Modellierung: Grundlagen und Anwendungen bei Strömungsprozessen*. Springer-Verlag, 2012.
[21] Daniel Stoll et al. "Investigation of aerodynamic drag in turbulent flow conditions". In: *SAE International Journal of Passenger Cars-Mechanical Systems* 9.2016-01-1605 (2016), pp. 733–742.
[22] Universidad Politècnica de València. *Wall functions*. https://cfd.blogs.upv.es/turbulence/wall-functions/.
[23] David C. Wilcox. *Turbulence Modelling for CFD*. Ed. by Inc. DCW Industries. 2006.
[24] Yiming Yin. "Current study on active flow control and passive flow control". In: (Dec. 2023).

**DEPARTMENT OF Mechanics and Maritime Science**
**CHALMERS UNIVERSITY OF TECHNOLOGY**
Gothenburg, Sweden
www.chalmers.se


CHALMERS
UNIVERSITY OF TECHNOLOGY